

# Perceive-IR: Learning to Perceive Degradation Better for All-in-One Image Restoration

Xu Zhang , Jiaqi Ma , Guoli Wang , Qian Zhang , Huan Zhang , *Member, IEEE*, and Lefei Zhang , *Senior Member, IEEE*

**Abstract**—Existing All-in-One image restoration methods often fail to perceive degradation types and severity levels simultaneously, overlooking the importance of fine-grained quality perception. Moreover, these methods often utilize highly customized backbones, which hinder their adaptability and integration into more advanced restoration networks. To address these limitations, we propose Perceive-IR, a novel backbone-agnostic All-in-One image restoration framework designed for fine-grained quality control across various degradation types and severity levels. Its modular structure allows core components to function independently of specific backbones, enabling seamless integration into advanced restoration models without significant modifications. Specifically, Perceive-IR operates in two key stages: 1) multi-level quality-driven prompt learning stage, where a fine-grained quality perceiver is meticulously trained to discern three-tier quality levels by optimizing the alignment between prompts and images within the CLIP perception space. This stage ensures a nuanced understanding of image quality, laying the groundwork for subsequent restoration; 2) restoration stage, where the quality perceiver is seamlessly integrated with a difficulty-adaptive perceptual loss, forming a quality-aware learning strategy. This strategy not only dynamically differentiates sample learning difficulty but also achieves fine-grained quality control by driving the restored image toward the ground truth while pulling it away from both low- and medium-quality samples. Furthermore, Perceive-IR incorporates a Semantic Guidance Module (SGM) and Compact Feature Extraction (CFE). The SGM leverages semantic information from pre-trained vision models to provide high-level contextual guidance, while the CFE focuses on extracting degradation-specific features, ensuring accurate handling of diverse image degradations. Extensive experiments demonstrate that Perceive-IR not only surpasses state-of-the-art methods but also generalizes reliably to zero-shot real-world and unknown degraded scenes, while adapting seamlessly to different backbone networks. This versatility underscores the framework’s robustness and backbone-agnostic design.

**Index Terms**—All-in-One image restoration, Degradation perception, Quality-aware learning, Backbone-agnostic.

This work was supported by the National Natural Science Foundation of China under Grant 62431020, the Foundation for Innovative Research Groups of Hubei Province under Grant 2024AFA017, and the Fundamental Research Funds for the Central Universities under Grant 2042025kf0030. (Xu Zhang and Jiaqi Ma contributed equally to this work.) (Corresponding author: Lefei Zhang.)

Xu Zhang and Lefei Zhang are with the National Engineering Research Center for Multimedia Software, School of Computer Science, Wuhan University, Wuhan 430072, China (e-mail: zhangx0802@whu.edu.cn; zhanglefei@whu.edu.cn).

Jiaqi Ma is with the School of Computer Science, Wuhan University, Wuhan 430072, China, and also with the Mohamed bin Zayed University of Artificial Intelligence, UAE (e-mail: jiaqima@whu.edu.cn).

Guoli Wang and Qian Zhang are with the Horizon Robotics, Beijing 100083, China (e-mail: guoli.wang@horizon.cc; qian01.zhang@horizon.ai).

Huan Zhang is with the School of Information Engineering, Guangdong University of Technology, Guangzhou 510006, China (e-mail: huanzhang2021@gdut.edu.cn).

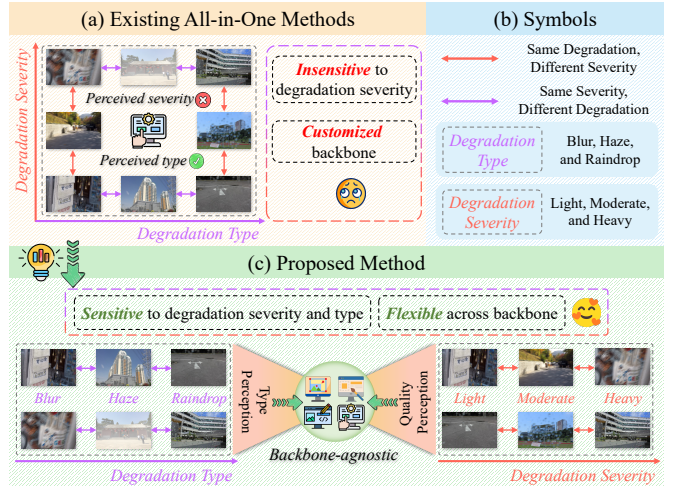


Fig. 1. Mechanisms of existing All-in-One methods vs. our method. (a) Existing All-in-One methods are capable of recognizing degradation types (such as blur, haze, etc.) but struggle to perceive severity levels, often only distinguishing between light and heavy cases. Furthermore, their reliance on customized backbones further limits transferability. (b) Legend for symbols. (c) Our method simultaneously perceives degradation types and severity levels, while being compatible with diverse restoration backbones, offering superior flexibility and versatility.

## I. INTRODUCTION

IMAGE restoration, the process of recovering a clear image from its degraded version, has seen remarkable advancements with the emergence of deep learning. Traditionally, this challenge has been addressed by task-specific networks, each specifically designed and trained to handle a unique type of degradation. This targeted approach has yielded significant success across a spectrum of restoration tasks, *e.g.*, denoising [1]–[3], dehazing [4]–[6], deraining [7]–[9], deblurring [10]–[12], and low-light enhancement [13]–[15].

Although task-specific methods have proven effective, their applicability is inherently restricted because they are designed to address specific types of degradation. Once switched to other degradation scenarios, the effectiveness of these methods diminishes significantly. To overcome these limitations, general image restoration methods [16]–[21] have been introduced. These methods are capable of handling various types of degradation, but they typically require separate models for each degradation type, making the inference stage resource-intensive and impractical.

Recently, All-in-One image restoration methods [22]–[33] have emerged as a potential solution to these challenges. These methods can handle multiple degradation types con-

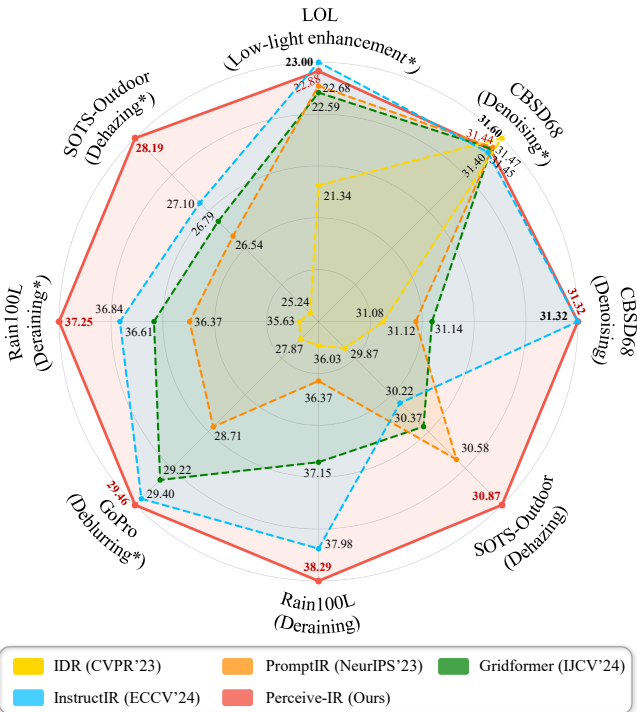


Fig. 2. PSNR comparisons with state-of-the-art All-in-One methods across two common All-in-One image restoration scenarios. \* denotes results obtained under All-in-One (“Noise+Haze+Rain+Blur+Low-light”) training setting, while unmarked results are from All-in-One (“Noise+Haze+Rain”) training setting. Our method’s results are marked in red, while the best results are indicated in bold.

currently by employing various mechanisms. Early works, such as AirNet [23], obtained discriminative representations of degraded features by explicitly constructing degradation encoders. Later methods, like ProRes [26] and PromptIR [27], further improved restoration performance by injecting visual prompt information. More recent studies [24], [29] have leveraged the feature representation capabilities of large-scale visual models like CLIP [34] and DINO [35] to enhance texture reconstruction and maintain structural consistency.

Despite these advances, a significant challenge remains in accurately mapping degraded images, which exhibit varying degrees of distortion, to their corresponding ground truths. This challenge is particularly pronounced in terms of fine-grained quality perception and the ability to adapt to diverse degradation severities. As illustrated in Fig. 1, existing All-in-One restoration methods are capable of recognizing degradation types but often struggle to perceive the severity levels of degradation. These methods typically rely on customized backbones, which limit their transferability. In contrast, our proposed method is sensitive to both degradation severity and type while being flexible across different restoration models.

To achieve this, we introduce two key insights. First, we propose a quality-aware learning strategy that enables fine-grained quality control and dynamic adaptation to varying degradation levels. Second, we incorporate a Semantic Guidance Module (SGM) and Compact Feature Extraction (CFE). The SGM leverages semantic cues from large-scale vision models to provide high-level contextual guidance, while the CFE focuses on extracting degradation-specific features, enabling the model

to perceive different types of degradation.

As demonstrated in Fig. 2, Perceive-IR outperforms existing state-of-the-art All-in-One restoration methods, exhibiting superior performance across various degradation scenarios.

Our contributions can be summarized as follows:

- We introduce Perceive-IR, a versatile All-in-One image restoration framework that not only perceives both degradation types and fine-grained severity levels but also achieves remarkable transferability to various restoration models.
- We design the quality-aware learning strategy, which is based on a CLIP-aware loss and difficulty-adaptive perceptual loss, to enable fine-grained quality control and dynamic differentiation of sample learning difficulty. This strategy drives the restored image toward the ground truth while pulling it away from both low- and medium-quality samples.
- We develop a novel semantic guidance module that combines a pre-trained DINO-v2 model with a prompt guidance module, generating feature representations enriched with both high-level semantic priors and degradation-specific cues, thereby significantly enhancing the restoration process.
- Extensive results demonstrate that Perceive-IR achieves state-of-the-art performance across diverse image restoration tasks. Importantly, it is inherently backbone-agnostic, seamlessly adapting to various restoration models, making it a highly flexible framework for All-in-One image restoration.

## II. RELATED WORK

### A. All-in-One Restoration

All-in-One restoration [22]–[33], which aims to recover clean images from multiple degradations through a unified model, has grown to be a promising field of low-level vision tasks. Compared to task-specific [1], [2], [4]–[15], [36]–[38] and general [16]–[21], [39], [40] image restoration, All-in-One restoration is more advantageous in terms of model storage efficiency and practical applications. The main challenge lies in using a single set of model parameters to handle various types of degradation and accurately restore the corresponding components. To achieve this, AirNet [23] proposed learning discriminative degradation representation using contrastive learning. IDR [25] took a different approach by utilizing a two-stage ingredients-oriented restoration network. PromptIR [27] and ProRes [26] further enhanced the network’s ability to handle multiple degradation through vision prompts. More recently, CLIP-AWR [24], DA-CLIP [31], and DINO-IR [29] leveraged pre-trained large-scale vision models to excel in All-in-One restoration tasks.

However, in practice, degraded images often suffer from varying levels of corruption. The above methods may fall into the trap of processing these images with the same restoration effort, resulting in sub-optimal performance. Based on this observation, Chen *et al.* [30] designed a blind All-in-One image restoration method by learning an image quality ranker. However, it depends on the simple image quality metric, *i.e.*, PSNR, and is susceptible to variations in certain parameters. Furthermore, most of these methods rely on highly customized backbones, which compromises model flexibility. In contrast, our approach incorporates a quality-aware learning strategy

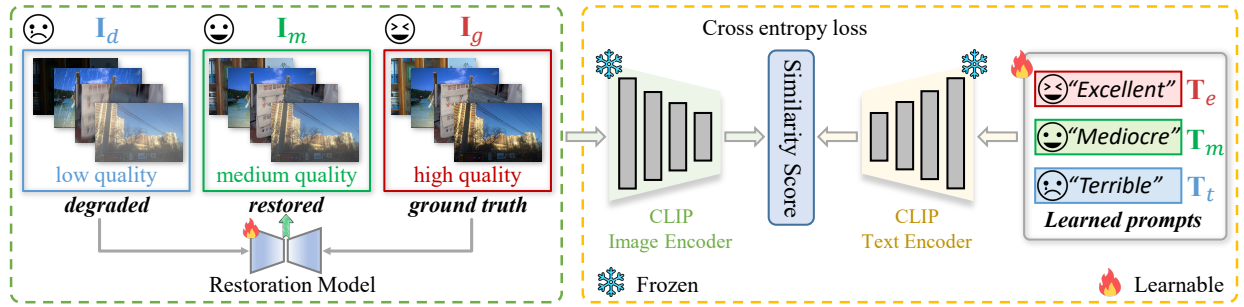


Fig. 3. In the proposed multi-level quality-driven prompt learning stage, we initialize and train textual prompts using image-text pairs categorized into three tiers of quality. The medium quality images are obtained by training the restoration model (e.g., Restormer [19]) using a cross-validation strategy. Then, these image-text pairs are trained with cross-entropy loss in the CLIP model. Once trained, the learned prompts are fixed and used to guide the restoration of high-quality images during the subsequent restoration stage.

and compact feature extraction to achieve fine-grained quality control and uncover degradation-specific cues. This demonstrates superior sensitivity to both the severity and type of degradation, while maintaining remarkable adaptability across various restoration models.

### B. Prompt Learning

In recent years, prompt learning as an emerging learning paradigm has seen significant advancements in the field of natural language processing [41]. Its effectiveness has led to its widespread application in vision-related tasks [42]. The core idea is to enable pre-trained models to better understand and perform downstream tasks by constructing specific prompts. In natural language processing, these prompts are usually given in the form of text, whereas in computer vision, they may involve images, text, or other forms of data. Recently, CLIP-LIT [43] has shown that initializing textual prompts in CLIP can aid in extracting more accurate low-level image representations. However, relying solely on distinguishing between positive and negative prompts may fail to effectively guide the restoration process towards achieving undistorted images. This is because the vast spectrum of possibilities between the two prompts can complicate the accurate mapping of degraded images to their pristine counterparts. To address this, we propose a multi-level quality-driven prompt learning stage that further refines the differentiation among three-tier prompt pairs. This approach enables more nuanced and precise control over the restoration process, ensuring a more accurate alignment with undistorted images.

### C. Large-scale Vision Models

Large-scale vision models (LVMs) have demonstrated powerful robust feature representation and zero-shot transfer capabilities across various tasks. For example, CLIP [34] has been widely adopted in numerous downstream applications due to its remarkable ability to align semantic information between vision and language. Similarly, self-supervised ViT models like DINO [35] and DINO-v2 [44] have proven effective in multiple domains, eliminating the need for labeled input data. Given that these LVMs can extract valuable prior knowledge from external hyper-scale datasets, leveraging pre-trained LVMs has become increasingly popular in the low-level vision community [24], [29], [31]. Inspired by these

advancements, our work utilizes the semantic prior knowledge and structural information extracted by the proposed DINO-v2-based semantic guidance module to guide the restoration process.

## III. METHOD

### A. Overview Pipeline

Our Perceive-IR contains two stages: a prompt learning stage and a restoration stage. In the prompt learning stage, we initialize and train textual prompts using image-text pairs categorized into three-tier quality by constraining the text-image similarity in the CLIP perception space. The learned prompts are fixed and then used to guide the restoration process during the subsequent stage. In the restoration stage, we use compact feature extraction (CFE) to learn distinct degradation representations. These representations are then concatenated with semantic priors extracted by pre-trained DINO-v2 encoder. These concatenated features modulate the output features of the decoder within the prompt guidance module (PGM). The calibrated features are further processed by the prior guidance cross attention (PGCA) to emphasize and extract structural semantic information and convey it. Moreover, we utilize the quality-aware learning strategy which contains CLIP-aware loss and difficulty-adaptive perceptual loss to realize fine-grained quality control and guide the restoration of high-quality images.

### B. Multi-level Quality-Driven Prompt Learning Stage

The process of multi-level quality-driven prompt learning stage is shown in Fig. 3. We use the CLIP model to learn three types of prompts: “terrible”, “mediocre”, and “excellent”, which correspond to the three-tier quality levels (low, medium, and high) of images processed by the CLIP image encoder. Specifically, we divide the degraded inputs equally into two subsets. Then, we train a restoration model, *i.e.*, Restormer [19] to obtain the restored images  $I_m$  via cross-validation strategy. The restored images are regarded as medium quality images. After that, given a low quality degraded image  $I_d \in \mathbb{R}^{H \times W \times 3}$ , a medium quality restored image  $I_m \in \mathbb{R}^{H \times W \times 3}$ , and a high quality ground truth  $I_g \in \mathbb{R}^{H \times W \times 3}$ , we randomly initialize a “terrible” textual prompt  $T_t \in \mathbb{R}^{N \times 512}$ , a “mediocre” textual prompt  $T_m \in \mathbb{R}^{N \times 512}$ , and an “excellent”

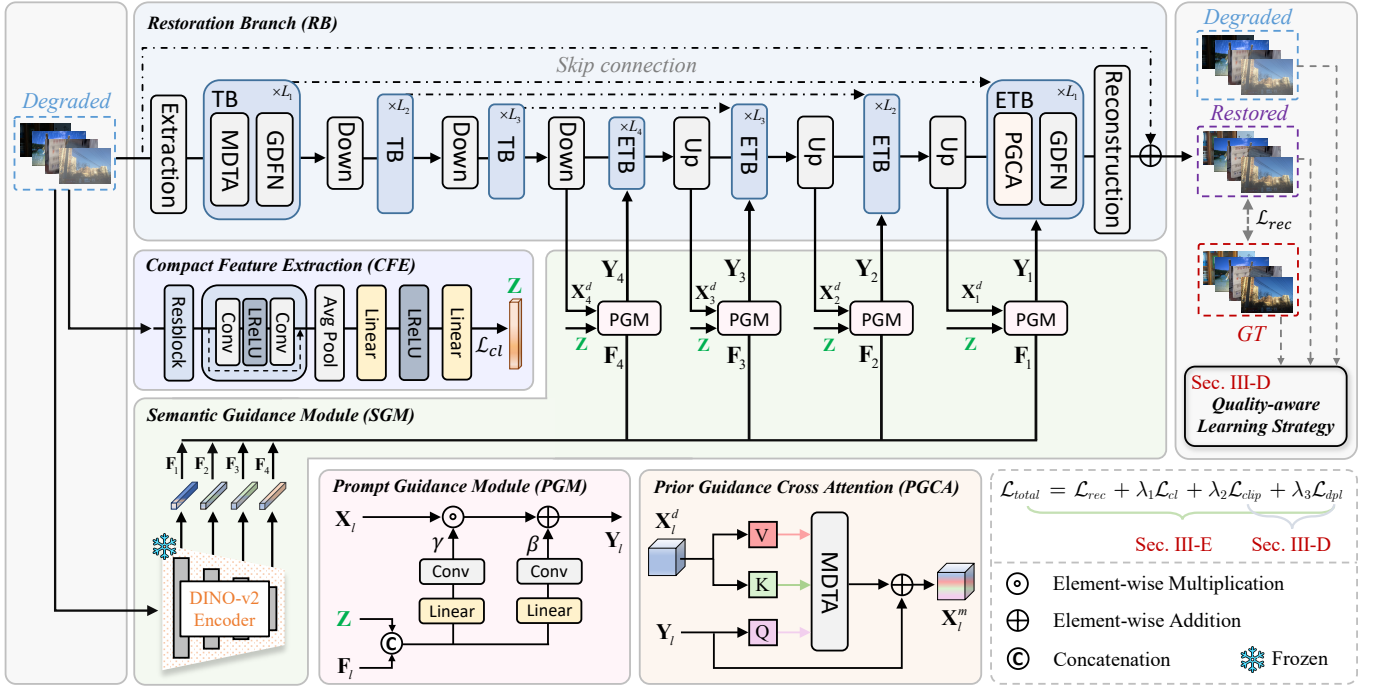


Fig. 4. The proposed restoration stage consists of: (a) Restoration Branch (RB): A 4-level U-shaped encoder-decoder structure that incorporates Transformer Block (TB) [19] in the encoder and Enhanced Transformer Block (ETB) in the decoder. (b) Compact Feature Extraction (CFE): A module designed to generate distinctive degradation representation. (c) Semantic Guidance Module (SGM): Comprising a pre-trained DINO-v2 [44] and the Prompt Guidance Module (PGM) to produce feature representations enriched with semantic and degradation priors.

textual prompt  $\mathbf{T}_e \in \mathbb{R}^{N \times 512}$ .  $N$  represents the number of embedded tokens in each prompt. Then, we feed the low, medium, and high quality images  $\mathbf{I}_d$ ,  $\mathbf{I}_m$ , and  $\mathbf{I}_g$  to the CLIP image encoder to obtain their latent encoding. Meanwhile, we extract the latent encodings of the “excellent”, “mediocre”, and “terrible” textual prompts by feeding them to the CLIP text encoder. Based on the text-image similarity in the CLIP latent space, we use the cross entropy loss  $\mathcal{L}_{ce}$  of classifying the low, medium, and high quality images to learn these prompts. The  $\mathcal{L}_{ce}$  can be described as

$$\mathcal{L}_{ce} = -\frac{1}{3} \sum_{i \in \{d, m, g\}} \sum_{j \in \{e, m, t\}} \mathcal{Y}_{ij} \log \left( \frac{\exp(\mathcal{S}(\Phi_{\mathcal{I}}(\mathbf{I}_i), \Phi_{\mathcal{T}}(\mathbf{T}_j)))}{\sum_{k \in \{e, m, t\}} \exp(\mathcal{S}(\Phi_{\mathcal{I}}(\mathbf{I}_i), \Phi_{\mathcal{T}}(\mathbf{T}_k)))} \right), \quad (1)$$

where  $\mathcal{S}(\cdot, \cdot)$  denotes cosine similarity and  $\mathcal{Y}_{ij}$  is the label of the current image  $\mathbf{I}_i$ ;  $\Phi_{\mathcal{I}}(\cdot)$  and  $\Phi_{\mathcal{T}}(\cdot)$  denote CLIP image encoder and CLIP text encoder, respectively.

### C. Restoration Stage

1) *Restoration Branch*: As shown in Fig. 4, given a degraded input  $\mathbf{I}_d \in \mathbb{R}^{H \times W \times 3}$ , we first apply a  $3 \times 3$  convolution to extract shallow embeddings  $\mathbf{X}_s \in \mathbb{R}^{H \times W \times C}$ , where  $H \times W$  denotes the spatial dimension and  $C$  is the number of channels. Next, the shallow features  $\mathbf{X}_s$  are gradually and hierarchically encoded into deep features  $\mathbf{X}_l^{e,d} \in \mathbb{R}^{\frac{H}{2^{l-1}} \times \frac{W}{2^{l-1}} \times 2^{l-1}C}$ . After encoding the degraded input into latent features  $\mathbf{X}_4 \in \mathbb{R}^{\frac{H}{8} \times \frac{W}{8} \times 8C}$ , the decoder progressively recovers the high-resolution representations. Finally, a  $3 \times 3$  convolution is applied to reconstruct the image  $\mathbf{I}_r \in \mathbb{R}^{H \times W \times 3}$ .

In the restoration branch, we choose Restormer [19] as backbone. Specifically, in the encoder layer, we integrate Multi-Dconv Head Transposed Attention (MDTA) [19] and Gated-Dconv Feed-Forward Network (GDFN) [19] to jointly construct the Transformer Block (TB). In the latent and decoder layers, we introduce the Prior Guidance Cross Attention (PGCA) and GDFN to jointly construct the Enhanced Transformer Block (ETB). The process of restoration branch can be described as

$$\mathcal{F}_{tb}(\mathbf{X}_l^e) = \mathcal{F}_{gdfn}(\mathcal{F}_{mdta}(\mathbf{X}_l^e)), \quad (2)$$

$$\mathcal{F}_{etb}(\mathbf{X}_l^d, \mathbf{Y}_l) = \mathcal{F}_{gdfn}(\mathcal{F}_{pgca}(\mathbf{X}_l^d, \mathbf{Y}_l)), \quad (3)$$

$$\mathbf{I}_r = \text{Conv} \left( \mathcal{F}_{etb}^{4,3,2,1} \left( \mathcal{F}_{tb}^{1,2,3} (\text{Conv}(\mathbf{I}_d)) \downarrow_{\times 2}, \mathbf{Y}_l \right) \uparrow_{\times 2} \right) + \mathbf{I}_d, \quad (4)$$

where  $\mathcal{F}_{gdfn}(\cdot)$ ,  $\mathcal{F}_{mdta}(\cdot)$ ,  $\mathcal{F}_{pgca}(\cdot)$ ,  $\mathcal{F}_{tb}(\cdot)$ , and  $\mathcal{F}_{etb}(\cdot)$  indicate GDFN, MDTA, PGCA, TB, and ETB processes, respectively;  $\mathbf{X}_l^e$  denotes the output of  $l$ -th encoder layer and  $\mathbf{X}_l^d$  represents the input of  $l$ -th decoder layer, respectively;  $\text{Conv}(\cdot)$  indicates  $3 \times 3$  convolution operation and  $\mathbf{Y}_l$  denotes output of prompt guidance module;  $\downarrow$  and  $\uparrow$  indicate down-sampling and up-sampling, respectively.

2) *Compact Feature Extraction*: In the restoration stage, we propose Compact Feature Extraction (CFE) to extract a compact degradation representation  $\mathbf{Z} \in \mathbb{R}^{1 \times 128}$ . Then, we utilize the degradation loss  $\mathcal{L}_{cl}$  (as detailed in Sec. III-E) to optimize CFE by leveraging the consistency of images with the same degradation and the inconsistency across different degradation. After that,  $\mathbf{Z}$  will be concatenated with the multi-scale features  $\mathbf{F}_l$  extracted by pre-trained large vision model.

The deep feature  $\mathbf{X}_l^d$  and the concatenated feature will perform affine transformation in Prompt Guidance Module (PGM) to obtain  $\mathbf{Y}_l$ . Subsequently, the  $\mathbf{Y}_l$  is employed to execute cross-attention within the Enhanced Transformer Block (ETB).

3) *Semantic Guidance Module*: Recently, large-scale vision models (e.g., DINO family [35], [44]) have demonstrated their potential in a series of visual downstream tasks in a self-supervised manner. DINO-v2, as an improved version of DINO, can provide more powerful feature representation thanks to pre-training on more than one million data. To this end, we employ the DINO-v2 to extract useful semantic feature priors from degraded images. Additionally, a prompt guidance module (PGM) is designed to help the network better capture and preserve structural semantic information. As shown in Fig. 4, given a degraded image  $\mathbf{I}_d$ , it goes through the pre-trained DINO-v2 encoder and outputs four different levels of semantic features  $\mathbf{F}_l \in \mathbb{R}^{1 \times 768}$  ( $l = 1, 2, 3, 4$ ). This process can be described as

$$\mathbf{F}_1, \mathbf{F}_2, \mathbf{F}_3, \mathbf{F}_4 = \mathcal{D}_i(\mathbf{I}_d), \quad i = 1, 4, 8, 12, \quad (5)$$

where  $\mathcal{D}_i(\cdot)$  denotes the  $i$ -th layer of DINO-v2 encoder. Then, the semantic prior and learned degradation representation  $\mathbf{Z}$  are exploited to generate reliable content to guide the restoration by PGM. The modulated feature  $\mathbf{Y}_l$  is transmitted to prior guidance cross attention (PGCA) to guide the restoration branch. Specifically, we take  $\mathbf{Y}_l$  as query to perform the cross-attention. The above process can be expressed as

$$\mathbf{Y}_l = \mathcal{F}_{pgm}(\mathbf{F}_l, \mathbf{Z}, \mathbf{X}_l^d), \quad (6)$$

$$CrossAtt(\mathbf{Y}_l, \mathbf{X}_l^d, \mathbf{X}_l^d) = \text{Softmax}(\hat{\mathbf{Q}} \otimes \hat{\mathbf{K}}/\alpha) \otimes \hat{\mathbf{V}}, \quad (7)$$

$$\mathbf{X}_l^m = \mathcal{F}_{mpta}(CrossAtt(\mathbf{Y}_l, \mathbf{X}_l^d, \mathbf{X}_l^d)) + \mathbf{Y}_l, \quad (8)$$

where  $\mathcal{F}_{pgm}$  indicates PGM process;  $\otimes$  denotes matrix multiplication.

#### D. Quality-aware Learning Strategy

1) *CLIP-aware Loss*: As illustrated in Fig. 5, given the learned text prompts obtained from the prompt learning stage, we first fix these prompts and then train the restoration model using the CLIP-aware loss  $\mathcal{L}_{clip}$ . The  $\mathcal{L}_{clip}$  can be described as

$$\mathcal{L}_{clip} = 1 - \frac{\exp(\mathcal{S}(\Phi_{\mathcal{I}}(\mathbf{I}_r), \Phi_{\mathcal{T}}(\mathbf{T}_e)))}{\sum_{k \in \{e, m, t\}} \exp(\mathcal{S}(\Phi_{\mathcal{I}}(\mathbf{I}_r), \Phi_{\mathcal{T}}(\mathbf{T}_k)))}, \quad (9)$$

where  $\mathcal{S}(\cdot, \cdot)$  denotes cosine similarity. The  $\mathcal{L}_{clip}$  is to minimize the gap between the restored images  $\mathbf{I}_r$  and the “excellent” prompt  $\mathbf{T}_e$ , while maximizing the gap between  $\mathbf{I}_r$  with the “mediocre” prompt  $\mathbf{T}_m$  and “terrible” prompt  $\mathbf{T}_t$ , respectively. It emphasizes pulling the restored results closer to the ground truth, guiding the model to generate high-quality images.

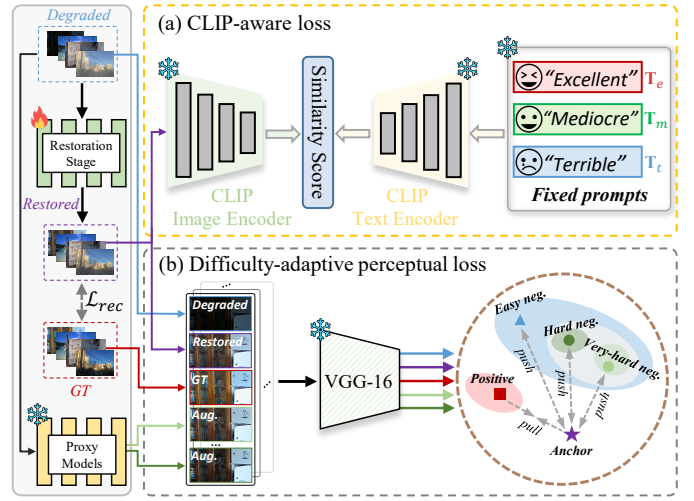


Fig. 5. The proposed quality-aware learning strategy contains two components: (a) The CLIP-aware loss penalizes the dissimilarity between the restored image and the “excellent” prompt, guiding the restored image to better resemble the ground truth; (b) The difficulty-adaptive perceptual loss dynamically adjusts its behavior based on the difficulty level of the restoration process by distinguishing the learning difficulty of samples in feature space.

2) *Difficulty-adaptive Perceptual Loss*: Using contrastive regularization has been demonstrated as an effective way of improving image restoration performance [45], [46]. Based on this, we introduce the difficulty-adaptive perceptual loss to dynamically adjust its behavior based on the difficulty level of the restoration process. It effectively handles both easy and hard samples, ensuring that the network focuses appropriately on challenging samples while efficiently processing easy cases. As shown in Fig. 5, the image predicted  $\mathbf{I}_r$  by the network serves as the anchor, the reference image  $\mathbf{I}_g$  is used as positive sample, the degraded  $\mathbf{I}_d$  is used as easy negative sample, and the augmented images  $\mathbf{I}_q$  from proxy restoration models (e.g., InstructIR [33], PromptIR [27], FSNet [20], and MambaIR [40]) as hard or very-hard negative samples.

Specifically, at the beginning of the  $k$ -th epoch, we evaluate the performance of network by calculating the average PSNR score and categorize the non-easy negative sample as a very-hard sample if its PSNR surpasses the current network performance, otherwise, it is classified as hard negative sample. Then, the weight  $\mathcal{O}_k$  of the  $k$ -th epoch assigned to a non-easy negative sample  $\mathcal{N}_q$ , is defined as

$$\mathcal{O}_k(\mathcal{N}_q) = \begin{cases} 1 + \gamma, & \text{avgPSNR}(\mathbf{I}_r, \Theta_{k-1}) \geq \text{PSNR}(\mathcal{N}_q), \\ 1 - \gamma, & \text{otherwise,} \end{cases} \quad (10)$$

where  $q = 1, 2, \dots, z$ ;  $z$  is the number of non-easy negatives, and  $\gamma$  is a hyperparameter set to 0.25;  $\Theta_{k-1}$  represents the model weights from the  $(k-1)$ -th epoch. The weights of hard and very-hard negatives are set to  $1 + \gamma$  and  $1 - \gamma$ , respectively. Based on this, the proposed  $\mathcal{L}_{dpl}$  can be written as

$$\mathcal{L}_{dpl} = \sum_{i=3,7,11,15} \xi_i \frac{\mathcal{M}_i(\mathbf{I}_g, \mathbf{I}_r)}{\lambda \mathcal{M}_i(\mathbf{I}_d, \mathbf{I}_r) + \sum_{q=1}^z \mathcal{O}_k(\mathcal{N}_q) \mathcal{M}_i(\mathcal{N}_q, \mathbf{I}_r)}, \quad (11)$$

where  $\mathcal{M}_i(\cdot, \cdot) = \|\mathcal{V}_i(\cdot) - \mathcal{V}_i(\cdot)\|_1$ ;  $\mathcal{V}_i(\cdot)$  represents the  $i$ -th latent feature extracted from the pre-trained VGG-16. We use the latent features of 3rd, 7-th, 11-th, 15-th layers from

TABLE I  
DATASET SUMMARY UNDER TWO TRAINING SETTINGS.

Setting	Degradation	Training dataset (Number)	Testing dataset (Number)
One-by-One (Single-task)	Noise (N)	N: BSD400 [47]+WED [48] (400+4744)	N: CBSD68 [49]+Urban100 [50]+Kodak24 [51] (68+100+24)
	Haze (H)	H: RESIDE- $\beta$ -OTS [52] (72135)	H: SOTS-Outdoor [52] (500)
	Rain (R)	R: Rain100L [53] (200)	R: Rain100L [53] (100)
	Blur (B)	B: GoPro [11] (2103)	B: GoPro [11] (1111)
	Low-Light (L)	L: LOL [13] (485)	L: LOL [13] (15)
All-in-One (Multi-task)	N+H+R	BSD400 [47]+WED [48]+RESIDE- $\beta$ -OTS [52]+Rain100L [53] Number: 400+4744+72135+200 Total: 77479	N: CBSD68 [49] (68) H: SOTS-Outdoor [52] (500) R: Rain100L [53] (100)
	N+H+R+B+L	BSD400 [47]+WED [48]+RESIDE- $\beta$ -OTS [52]+Rain100L [53] +GoPro [11]+LOL [13] Number: 400+4744+72135+200+2103+485 Total: 80067	N: CBSD68 [49] (68) H: SOTS-Outdoor [52] (500) R: Rain100L [53] (100) B: GoPro [11] (1111) L: LOL [13] (15)

VGG-16 to calculate  $\mathcal{M}_i(\cdot, \cdot)$ . We assign a fixed weight  $\lambda$  to the easy negative and set  $\lambda = 2$ .  $\{\xi_i\}$  represents the set of hyperparameters. We set  $\xi_i$  ( $i = 3, 7, 11, 15$ ) to  $\frac{1}{12}, \frac{1}{6}, \frac{1}{3}$ , and 1, respectively.

### E. Training Loss

In the prompt learning stage, we use  $\mathcal{L}_{ce}$  to learn the initial text prompt pairs. In the restoration stage, we first utilize Compact Feature Extraction (CFE) and introduce a degradation-aware loss  $\mathcal{L}_{cl}$  to learn degradation representations. The  $\mathcal{L}_{cl}$  can be written as

$$\mathcal{L}_{cl} = -\log \frac{\exp(\mathcal{S}(\mathbf{Z}, \mathbf{Z}^+)/\tau)}{\exp(\mathcal{S}(\mathbf{Z}, \mathbf{Z}^+)/\tau) + \sum_{i=1}^n \exp(\mathcal{S}(\mathbf{Z}, \mathbf{Z}_i^-)/\tau)}, \quad (12)$$

where  $n$  denotes the number of negative samples, and  $\tau$  indicates the temperature, which is set to 0.1. Given several images containing different degradation types, we randomly crop two patches of the same resolution on an image and let them be positive samples, while letting patches of different degradation types be negative samples. Then, feed them into CFE to get the anchor feature  $\mathbf{Z}$ , the positive feature  $\mathbf{Z}^+$ , and the negative feature  $\mathbf{Z}^-$ .

The total loss of the restoration stage can be described as

$$\mathcal{L}_{total} = \mathcal{L}_{rec} + \lambda_1 \mathcal{L}_{cl} + \lambda_2 \mathcal{L}_{clip} + \lambda_3 \mathcal{L}_{dpl}, \quad (13)$$

where  $\mathcal{L}_{rec}$  is the  $\mathcal{L}_1$  norm loss;  $\lambda_1$ ,  $\lambda_2$ , and  $\lambda_3$  are hyperparameters to make a balance of the total loss.

## IV. EXPERIMENTS

### A. Experimental Setup

1) *Datasets*: Following [23], [25], [27], we differentiate the training setups into “All-in-One” and “One-by-One” based on whether datasets are combined for mixed training. In our study, we summarise two common settings of mixed degradations: “Noise+Haze+Rain (N+H+R)” and “Noise+Haze+Rain+Blur+Low-light (N+H+R+B+L)”. Under the “One-by-One” setting, the model is trained and tested using datasets from a single image restoration task at a time. Under the “All-in-One” setting, the model is trained and tested using mixed datasets from multiple image restoration tasks.

In Tab. I, we detail the training and testing datasets used in our experiments. For single-task image restoration, **i**) Image denoising: we conduct training using a merged dataset of BSD400 [47] and WED [48] with 400 and 4,744 clear images, respectively. Noisy images are generated with Gaussian noise ( $\sigma \in \{15, 25, 50\}$ ). Testing is performed on CBSD68 [49], Urban100 [50], and Kodak24 [51] datasets. **ii**) Image dehazing: we use the OTS dataset of RESIDE- $\beta$  [52] with 72,135 pairs for training and 500 images from SOTS-Outdoor [52] dataset for testing. **iii**) Image deraining: we use the Rain100L [53] dataset with 200 pairs of images for training and 100 pairs for testing. **iv**) Image deblurring: we train the model on the GoPro [11] dataset, which contains 2,103 pairs for training and 1,111 pairs for testing. **v**) Low-light enhancement: we use the LOL [13] dataset, which contains 485 pairs for training and 15 pairs for testing. For multi-task image restoration, we train on a mixed dataset containing multiple degradations and test one by one on the dataset containing a single type of degradation.

2) *Evaluation Metrics*: We evaluate performance using reference metrics, including Peak Signal-to-Noise Ratio (PSNR), Structural Similarity Index (SSIM), and Learned Perceptual Image Patch Similarity (LPIPS) [54], as well as non-reference metrics such as the Underwater Colour Image Quality Evaluation Metric (UCIQE) [55], Underwater Image Quality Measure (UIQM) [56], Multi-scale Image Quality Transformer (MUSIQ) [57], Fog Aware Density Evaluator (FADE) [58], Blind/Referenceless Image Spatial Quality Evaluator (BRISQUE) [59], and Neural Image Assessment (NIMA) [60]. Among these, UCIQE and UIQM are specifically designed for evaluating underwater image restoration tasks, while FADE, BRISQUE, and NIMA are used to assess the performance of dehazing in real-world scenarios. For the metrics PSNR, SSIM, UCIQE, UIQM, MUSIQ, and NIMA, higher scores indicate better performance. In contrast, for the LPIPS, FADE, and BRISQUE metrics, lower scores are preferred. In the tables, the best and second-best scores are highlighted in **bold** and underlined, respectively.

3) *Baselines*: In the All-in-One (“N+H+R”) setting, we select four task-specific methods: LPNet [61], ADFNet [3], DehazeFormer [6], and DRSformer [9]; five general methods: MPRNet [16], Restormer [19], NAFNet [18], FSNet [20],

and MambaIR [40], and seven All-in-One methods: DL [62], AirNet [23], IDR [25], NDR [28], PromptIR [27], Gridformer [32] and InstructIR [33]. In the All-in-One (“N+H+R+B+L”) setting, we add task-specific methods like HI-Diff [63] and Retinexformer [15]; general methods such as DGUNet [39], and MIRNet-v2 [17]; as well as All-in-One methods like Transweather [64], and TAPE [22].

In the One-by-One setting, we focus on adjustments to task-specific methods. For denoising, we employ DnCNN [1], FFDNet [2], and ADFNet [3]. For dehazing, we utilize DehazeNet [4], AODNet [65], FDGAN [5], and DehazeFormer [6]. For deraining, we apply UMR [7], MSPFN [8], LPNet [61], and DRSformer [9]. For image deblurring, we leverage DeblurGAN [10], Stripformer [12], and HI-Diff [63]. Lastly, for low-light image enhancement, we incorporate Retinex-Net [13], URetinex [14], and Retinexformer [15]. In addition to these methods, we also report results from some representative general and All-in-One methods trained in the One-by-One setting.

4) *Implementation Details*: For the prompt learning stage, we employ the CLIP model with ViT-B/32 as the backbone. We train Restormer [19] for 100K iterations with a learning rate of  $2 \times 10^{-4}$ . The number of embedded tokens  $N$  in each learnable prompt is set to 16, and the prompt initialization is set to 100K iterations with a learning rate of  $4 \times 10^{-5}$  and the batch size is set to 32. For the restoration stage, we chose Restormer as the restoration backbone of Perceive-IR and DINO-v2 [44] base version as the semantic guidance module. We adopt a similar setting to the original Restormer. From level-1 to level-4, the numbers of TB and ETB are [4, 6, 6, 8], attention heads in MDTA and PGCA are both [1, 2, 4, 8], and the channel numbers are [48, 96, 192, 384]. We utilize AdamW optimizer with  $\beta_1 = 0.9$  and  $\beta_2 = 0.999$  to optimize the network. The learning rate is set to  $2 \times 10^{-4}$  with a total batch size of 6 for 400K iterations. The weighting parameters for  $\mathcal{L}_{total}$  are:  $\lambda_1 = 0.1$ ,  $\lambda_2 = 0.05$ , and  $\lambda_3 = 0.1$ . Following [27], given the substantial variation in data size across tasks (shown in Tab. I), we adopted task-specific resampling ratios to balance the training sets. Specifically, a resampling ratio of 3 was applied for denoising, 120 for deraining, 5 for deblurring, and 200 for low-light enhancement, while no resampling was performed for dehazing. All experiments are conducted on 8 NVIDIA GeForce RTX 3090 GPUs. During training, we utilize cropped patches of size  $128 \times 128$  as input, and random horizontal and vertical flips are applied to augment the training data.

## B. All-in-One Restoration Results

Tab. II presents the overall performance of Perceive-IR and other state-of-the-art methods under the All-in-One “N+H+R” training setting. It can be observed that the All-in-One methods basically perform better than general methods and task-specific methods. Particularly, in terms of overall performance, our Perceive-IR exhibits superior results compared with PromptIR [27] by over 0.57 dB/0.004 on average in PSNR/SSIM while utilizing the same backbone of Restormer [19]. Compared to the latest methods, Gridformer [32] and InstructIR [33],

Perceive-IR also demonstrates a PSNR/SSIM improvement of 0.44 dB/0.005 and 0.20 dB/0.004, respectively.

When extending to the more challenging “N+H+R+B+L” setting, as shown in Tab. III, Perceive-IR continues to demonstrate its superiority. Compared to PromptIR, Gridformer, and InstructIR, it achieves average PSNR/SSIM improvements of 0.69 dB/0.005, 0.51 dB/0.005, and 0.29 dB/0.002, respectively. Interestingly, as the number of degradation types increases, the performance gap between All-in-One methods and general image restoration methods narrows. By contrast, Perceive-IR still maintains good performance. Additionally, we report the performance of All-in-One methods on perceptual metrics, such as LPIPS [54] and MUSIQ [57]. As illustrated in Fig. 8, Perceive-IR achieves the lowest LPIPS scores (indicating higher perceptual similarity) and the highest MUSIQ scores (indicating better overall quality) across all datasets. For example, on the Rain100L dataset, Perceive-IR improves LPIPS by 12.5% and MUSIQ by 8.3% compared to the second-best method. These results highlight Perceive-IR’s ability to restore images with both high perceptual fidelity and overall quality, validating its effectiveness in diverse restoration scenarios.

## C. One-by-One Restoration Results

In this part, we evaluate Perceive-IR under One-by-One setting. As shown in Tab. IV, compared to the state-of-the-art (SOTA) task-specific denoising method ADFNet [3] and the SOTA general image restoration method FSNet [20], Perceive-IR surpasses them by 0.17 dB and 0.29 dB in PSNR, respectively, at a noise level of 15 on the CBSD68 and Urban100 datasets. As shown in Tab. V, while Perceive-IR demonstrates highly competitive performance in dehazing and deraining tasks, it does not perform as well as the best task-specific methods (*i.e.*, HI-Diff [63] and Retinexformer [15]) and the best general methods (*i.e.*, FSNet [20] and MIRNet [67]) on deblurring and low-light enhancement tasks. This limitation may stem from the fact that our method does not explicitly incorporate task-specific priors, which limits its ability to capture critical degradation features and adapt to diverse lighting and illumination conditions. Interestingly, when we replaced the restoration backbone with GRL [72] for deblurring and low-light enhancement tasks, we observed performance improvements of 0.11 dB and 0.12 dB, respectively. This adjustment not only demonstrates the adaptability of our framework but also underscores the importance of selecting an appropriate restoration backbone. These results suggest that while our method excels in generalizability, further integration of task-specific priors or backbone enhancements could bridge the performance gap in specialized tasks. A more detailed analysis is provided in Sec. IV-G.

## D. Generalization

In this section, we evaluate the generalization capabilities of various models, focusing on their zero-shot generalization in real-world scenarios as well as their ability to handle unknown degradation types and severity. Specifically, we select noise, haze, and rain as benchmark degradation types and evaluate them on their corresponding real-world datasets: SIDD val

TABLE II

PERFORMANCE COMPARISON IN **ALL-IN-ONE** (“**N+H+R**”) SETTING WITH **TASK-SPECIFIC**, **GENERAL**, AND **ALL-IN-ONE** IMAGE RESTORATION METHODS. THE REPORTED RESULTS ARE PARTIALLY BASED ON NDR [28] AND PROMPTIR [27]. \* DENOTES A MODEL THAT HAS BEEN RETRAINED.

Type	Method	Denoising (CBSD68 [49])			Dehazing	Deraining	Average	Params (M)
		$\sigma = 15$	$\sigma = 25$	$\sigma = 50$				
Specific	(CVPR’19) LPNet [61]	26.47/0.778	24.77/0.748	21.26/0.552	20.84/0.828	24.88/0.784	23.64/0.738	2.84
	(AAAI’23) ADFNet* [3]	33.76/0.929	30.83/0.871	27.75/0.793	28.13/0.961	34.24/0.965	30.94/0.904	7.65
	(TIP’23) DehazeFormer* [6]	33.01/0.914	30.14/0.858	27.37/0.779	29.58/0.970	35.37/0.969	31.09/0.898	25.44
	(CVPR’23) DRSformer* [9]	33.28/0.921	30.55/0.862	27.58/0.786	29.02/0.968	35.89/0.970	31.26/0.902	33.72
General	(CVPR’21) MPRNet [16]	33.27/0.920	30.76/0.871	27.29/0.761	28.00/0.958	33.86/0.958	30.63/0.894	15.74
	(CVPR’22) Restormer [19]	33.72/0.930	30.67/0.865	27.63/0.792	27.78/0.958	33.78/0.958	30.75/0.901	26.13
	(ECCV’22) NAFNet [18]	33.03/0.918	30.47/0.865	27.12/0.754	24.11/0.928	33.64/0.956	29.67/0.844	17.11
	(TPAMI’23) FSNet* [20]	33.81/0.930	30.84/0.872	27.69/0.792	29.14/0.968	35.61/0.969	31.42/0.906	13.28
	(ECCV’24) MambaIR* [40]	33.88/0.931	30.95/0.874	27.74/0.793	29.57/0.970	35.42/0.969	31.51/0.907	26.78
All-in-One	(TPAMI’19) DL [62]	33.05/0.914	30.41/0.861	26.90/0.740	26.92/0.391	32.62/0.931	29.98/0.875	2.09
	(CVPR’22) AirNet [23]	33.92/0.932	31.26/0.888	28.00/0.797	27.94/0.962	34.90/0.967	31.20/0.910	8.93
	(CVPR’23) IDR* [25]	33.89/0.931	31.32/0.884	28.04/0.798	29.87/0.970	36.03/0.971	31.83/0.911	15.34
	(ArXiv’23) ProRes [26]	32.10/0.907	30.18/0.863	27.58/0.779	28.38/0.938	33.68/0.954	30.38/0.888	370.63
	(NeurIPS’23) PromptIR [27]	33.98/0.933	31.31/0.888	28.06/0.799	30.58/0.974	36.37/0.972	32.06/0.913	32.96
	(TIP’24) NDR [28]	34.01/0.932	31.36/0.887	28.10/0.798	28.64/0.962	35.42/0.969	31.51/0.910	28.40
	(IJCV’24) Gridformer* [32]	33.93/0.931	31.37/0.887	28.11/0.801	30.37/0.970	37.15/0.972	32.19/0.912	34.07
	(ECCV’24) InstructIR-3D [33]	34.15/0.933	31.52/0.890	28.30/0.804	30.22/0.959	37.98/0.978	32.43/0.913	15.84
	<b>Perceive-IR (Ours)</b>	<b>34.13/0.934</b>	<b>31.53/0.890</b>	<b>28.31/0.804</b>	<b>30.87/0.975</b>	<b>38.29/0.980</b>	<b>32.63/0.917</b>	42.02



Fig. 6. Visual comparisons of Perceive-IR with state-of-the-art All-in-One methods under “**N+H+R**” setting. Zoom-in for best view.

TABLE III

PERFORMANCE COMPARISON IN **ALL-IN-ONE** (“**(N+H+R+B+L)**”) SETTING WITH STATE-OF-THE-ARTS **TASK-SPECIFIC**, **GENERAL**, AND **ALL-IN-ONE** IMAGE RESTORATION METHODS. FOLLOW [25], DENOISING RESULTS ARE REPORTED FOR THE NOISE LEVEL  $\sigma = 25$ . THE REPORTED RESULTS ARE PARTIALLY BASED ON IDR [25]. \* DENOTES A MODEL THAT HAS BEEN RETRAINED.

Type	Method	Denoising	Dehazing	Deraining	Deblurring	Low-Light	Average	Params (M)
		CBSD68 [49]	SOTS [52]	Rain100L [53]	GoPro [11]	LOL [13]		
Specific	(AAAI’23) ADFNet* [3]	31.15/0.882	24.18/0.928	32.97/0.943	25.79/0.781	21.15/0.823	27.05/0.871	7.65
	(TIP’23) DehazeFormer* [6]	30.89/0.880	25.31/0.937	33.68/0.954	25.93/0.785	21.31/0.819	27.42/0.875	25.44
	(CVPR’23) DRSformer* [9]	30.97/0.881	24.66/0.931	33.45/0.953	25.56/0.780	21.77/0.821	27.28/0.873	33.72
	(NeurIPS’23) HI-Diff* [63]	30.61/0.878	25.09/0.935	33.26/0.951	26.48/0.800	22.01/0.822	27.49/0.877	23.99
	(ICCV’23) Retinexformer* [15]	30.84/0.880	24.81/0.933	32.68/0.940	25.09/0.779	22.76/0.834	27.24/0.873	1.61
General	(TPAMI’22) MIRNet-v2 [17]	30.97/0.881	24.03/0.927	33.89/0.954	26.30/0.799	21.52/0.815	27.34/0.875	5.86
	(CVPR’22) DGUNet [39]	31.10/0.883	24.78/0.940	36.62/0.971	27.25/0.837	21.87/0.823	28.32/0.891	17.33
	(CVPR’22) Restormer [19]	31.49/0.884	24.09/0.927	34.81/0.962	27.22/0.829	20.41/0.806	27.60/0.881	26.13
	(ECCV’22) NAFNet [18]	31.02/0.883	25.23/0.939	35.56/0.967	26.53/0.808	20.49/0.809	27.76/0.881	17.11
	(TPAMI’23) FSNet* [20]	31.33/0.883	25.53/0.943	36.07/0.968	28.32/0.869	22.29/0.829	28.71/0.898	13.28
	(ECCV’24) MambaIR* [40]	31.41/0.884	25.81/0.944	36.55/0.971	28.61/0.875	22.49/0.832	28.97/0.901	26.78
All-in-One	(TPAMI’19) DL [62]	23.09/0.745	20.54/0.826	21.96/0.762	19.86/0.672	19.83/0.712	21.05/0.743	2.09
	(ECCV’22) TAPE [22]	30.18/0.855	22.16/0.861	29.67/0.904	24.47/0.763	18.97/0.621	25.09/0.801	1.07
	(CVPR’22) Transweather [64]	29.00/0.841	21.32/0.885	29.43/0.905	25.12/0.757	21.21/0.792	25.22/0.836	37.93
	(CVPR’22) AirNet [23]	30.91/0.882	21.04/0.884	32.98/0.951	24.35/0.781	18.18/0.735	25.49/0.846	8.93
	(CVPR’23) IDR [25]	<b>31.60/0.887</b>	25.24/0.943	35.63/0.965	27.87/0.846	21.34/0.826	28.34/0.893	15.34
	(NeurIPS’23) PromptIR* [27]	<u>31.47/0.886</u>	26.54/0.949	36.37/0.970	28.71/0.881	22.68/0.832	29.15/0.904	32.96
	(IJCV’24) Gridformer* [32]	31.45/0.885	26.79/0.951	36.61/0.971	29.22/0.884	22.59/0.831	29.33/0.904	34.07
	(ECCV’24) InstructIR-5D [33]	31.40/0.887	27.10/0.956	36.84/0.973	<b>29.40/0.886</b>	<b>23.00/0.836</b>	29.55/0.907	15.84
	<b>Perceive-IR (Ours)</b>	<b>31.44/0.887</b>	<b>28.19/0.964</b>	<b>37.25/0.977</b>	<b>29.46/0.886</b>	<u>22.88/0.833</u>	<b>29.84/0.909</b>	42.02

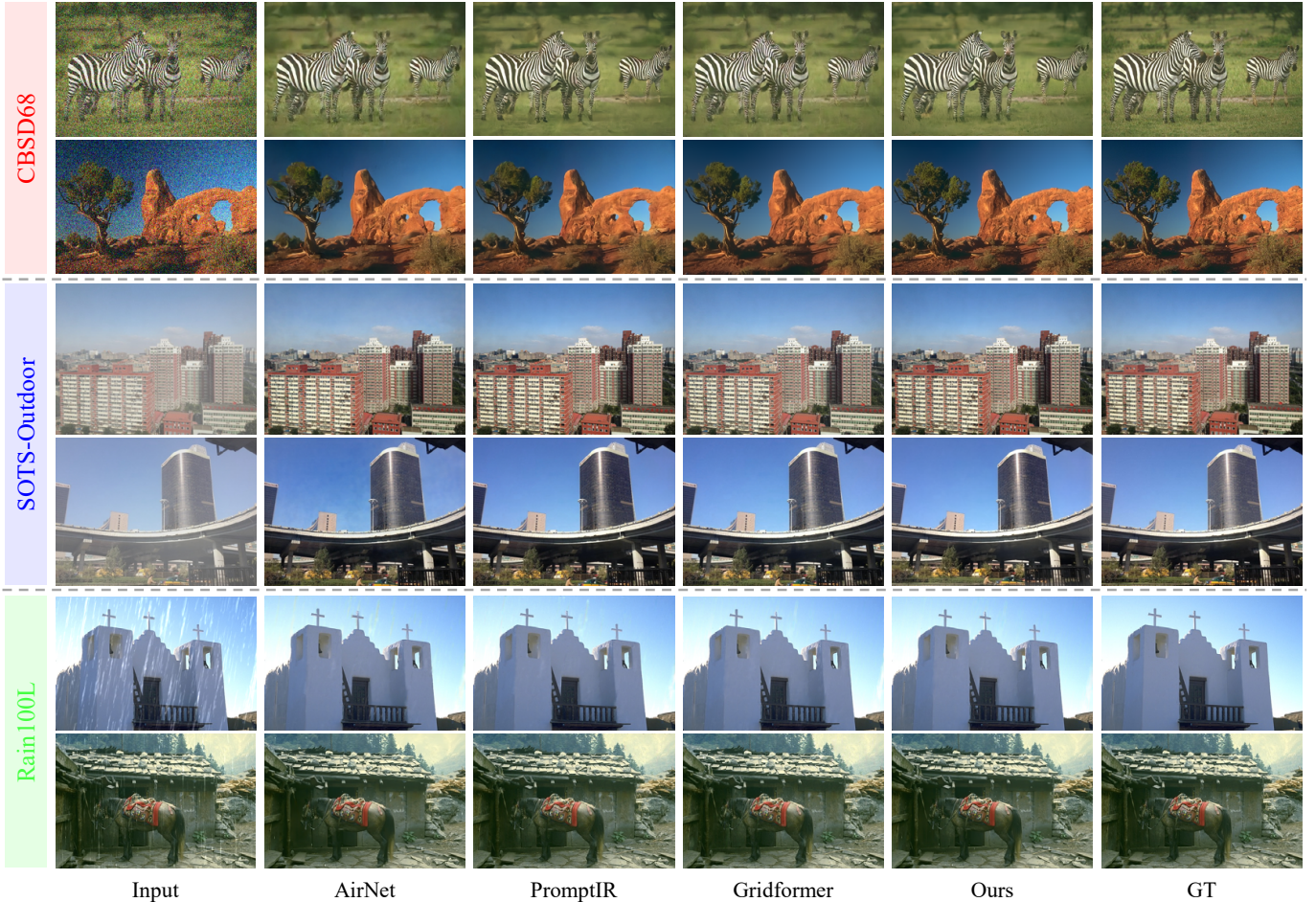


Fig. 7. Visual comparisons of Perceive-IR with state-of-the-art All-in-One methods under One-by-One setting. Zoom-in for best view.

TABLE IV

DENOISING PERFORMANCE COMPARISON IN THE **ONE-BY-ONE** SETTING ON **DENOISING** TASK.  $\diamond$ ,  $\diamond$ , AND  $\diamond$  DENOTE TASK-SPECIFIC, GENERAL, AND ALL-IN-ONE IMAGE RESTORATION METHODS, RESPECTIVELY. THE RESULTS IN THE TABLE ARE MAINLY BASED ON IDR [25].

Method	CBSD68 [49]			Urban100 [50]			Kodak24 [51]		
	15	25	50	15	25	50	15	25	50
$\diamond$ DnCNN [1]	33.90	31.24	27.95	32.98	30.81	27.59	34.60	32.14	28.95
$\diamond$ FFDNet [2]	33.87	31.21	27.96	33.83	31.40	28.05	34.63	32.13	28.98
$\diamond$ ADFNet* [3]	34.21	31.60	28.19	34.50	32.13	28.71	34.77	32.22	29.06
$\diamond$ MIRNet-v2 [17]	33.66	30.97	27.66	33.30	30.75	27.22	34.29	31.81	28.55
$\diamond$ DGUNet [39]	33.85	31.10	27.92	33.67	31.27	27.94	34.56	32.10	28.91
$\diamond$ Restormer [19]	34.03	31.49	28.11	33.72	31.26	28.03	34.78	32.37	29.08
$\diamond$ NAFNet [18]	33.67	31.02	27.73	33.14	30.64	27.20	34.27	31.80	28.62
$\diamond$ FSNet* [20]	34.09	31.55	28.12	33.88	31.31	28.07	34.75	32.38	29.10
$\diamond$ TAPE [22]	32.86	30.18	26.63	32.19	29.65	25.87	33.24	30.70	27.19
$\diamond$ AirNet [23]	34.14	31.48	28.23	34.40	32.10	28.88	34.81	32.44	29.10
$\diamond$ IDR [25]	34.11	31.60	28.14	33.82	31.29	28.07	34.78	<b>32.42</b>	<b>29.13</b>
$\diamond$ PromptIR [27]	34.34	31.71	28.49	34.77	32.49	29.39	-	-	-
$\diamond$ Perceive-IR	<b>34.38</b>	<b>31.74</b>	<b>28.53</b>	<b>34.86</b>	<b>32.55</b>	<b>29.42</b>	<b>34.84</b>	<b>32.50</b>	<b>29.16</b>

TABLE V

PERFORMANCE COMPARISON IN THE **ONE-BY-ONE** SETTING ON DEHAZING, DERAINING, DEBLURRING, AND LOW-LIGHT ENHANCEMENT TASKS.  $\diamond$ ,  $\diamond$ , AND  $\diamond$  DENOTE TASK-SPECIFIC, GENERAL, AND ALL-IN-ONE IMAGE RESTORATION METHODS, RESPECTIVELY. FOR LOW-LIGHT ENHANCEMENT, ALL-IN-ONE METHODS USE  $256 \times 256$  FOR TRAINING. THE BEST OVERALL RESULTS ARE MARKED WITH **BOLD** AND THE BEST RESULTS FROM EACH METHOD CATEGORY ARE IN **BOLD**.

Method	Dehazing SOTS [52]	Method	Deraining Rain100L [53]
$\diamond$ DehazeNet [4]	22.46/0.851	$\diamond$ UMR [7]	32.39/0.921
$\diamond$ AODNet [65]	20.29/0.877	$\diamond$ MSPFN [8]	33.50/0.948
$\diamond$ FDGAN [5]	23.15/0.921	$\diamond$ LPNet [61]	33.61/0.958
$\diamond$ DehazeFormer* [6]	<b>31.78/0.977</b>	$\diamond$ DRSformer* [9]	<b>38.14/0.983</b>
$\diamond$ Restormer [19]	30.87/0.969	$\diamond$ Restormer [19]	36.74/0.978
$\diamond$ NAFNet* [18]	30.98/0.970	$\diamond$ NAFNet* [18]	36.63/0.977
$\diamond$ FSNet* [20]	<b>31.11/0.971</b>	$\diamond$ FSNet* [20]	<b>37.27/0.980</b>
$\diamond$ AirNet [23]	23.18/0.900	$\diamond$ AirNet [23]	34.90/0.977
$\diamond$ PromptIR [27]	31.31/0.973	$\diamond$ PromptIR [27]	37.04/0.979
$\diamond$ Perceive-IR	<b>31.65/0.977</b>	$\diamond$ Perceive-IR	<b>38.41/0.984</b>
Method	Deblurring GoPro [11]	Method	Low-Light LOL [13]
$\diamond$ Nah <i>et al.</i> [11]	29.08/0.914	$\diamond$ Retinex-Net [13]	16.77/0.560
$\diamond$ DeblurGAN [10]	28.70/0.858	$\diamond$ URetinex [14]	21.33/0.835
$\diamond$ Stripformer [12]	33.08/0.962	$\diamond$ SMG [66]	23.81/0.809
$\diamond$ HI-Diff [63]	<b>33.33/0.964</b>	$\diamond$ Retinexformer [15]	<b>25.16/0.845</b>
$\diamond$ MPRNet [16]	32.66/0.959	$\diamond$ MIRNet [67]	<b>24.14/0.835</b>
$\diamond$ Restormer [19]	32.92/0.961	$\diamond$ Restormer [19]	22.43/0.823
$\diamond$ FSNet [20]	<b>33.29/0.963</b>	$\diamond$ DiffIR [21]	23.15/0.828
$\diamond$ AirNet* [23]	31.64/0.945	$\diamond$ AirNet* [23]	21.52/0.832
$\diamond$ PromptIR* [27]	32.41/0.956	$\diamond$ PromptIR* [27]	22.97/0.834
$\diamond$ Gridformer* [32]	32.59/0.957	$\diamond$ Gridformer* [32]	23.14/0.829
$\diamond$ Perceive-IR	32.83/0.960	$\diamond$ Perceive-IR	23.79/0.841
$\diamond$ Perceive-IR (GRL)	<b>32.94/0.961</b>	$\diamond$ Perceive-IR (GRL)	<b>23.91/0.843</b>

dataset [68] (for noise), RTTS [52] (for haze), and RealRain-1k-L test datasets [69] (for rain). Since the RTTS dataset lacks reference images, we additionally employed several non-reference metrics for quantitative comparison, such as FADE [58], BRISQUE [59], and NIMA [60].

1) *Zero-shot generalization in real-world scenes*: We evaluate the comparative methods trained under the “**N+H+R**” and “**N+H+R+B+L**” settings, directly assessing their zero-shot

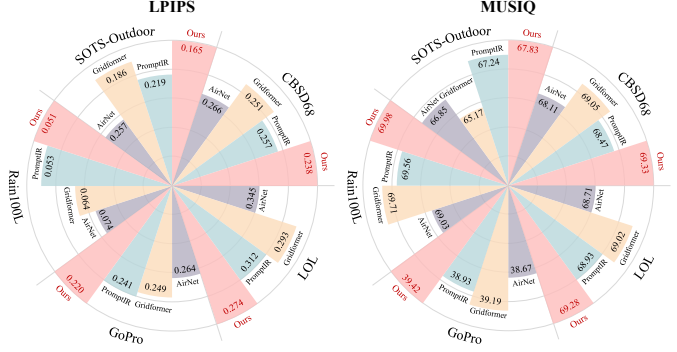


Fig. 8. A comparison of the LPIPS [54] and MUSIQ [57] perceptual metrics for the All-in-One methods under “**N+H+R+B+L**” setting.

generalization in real-world scenarios. As shown in Tab. VI, for noise removal on the SIDD dataset, Perceive-IR achieves 24.88 dB PSNR and 0.504 SSIM, outperforming InstructIR-7D (24.35/0.479) and PromptIR (24.58/0.482), demonstrating its robustness to unpredictable noise patterns. In hazy scenes from RTTS, Perceive-IR delivers superior perceptual quality with a FADE score of 1.213 (3.5% lower than InstructIR-7D), maintaining a competitive BRISQUE score of 21.621, and excelling in aesthetic assessment with a NIMA score of 4.681 (compared to 4.573 for InstructIR-7D), effectively addressing the common trade-off between distortion correction and visual naturalness in zero-shot setting. In addition, we conducted a series of fine-tuning experiments on several All-in-One approaches. Specifically, for real denoising tasks, we cropped 5,000 paired patches from 320 images in the SIDD training dataset; for real dehazing tasks, we cropped 3,925 paired patches from LMHaze [73] dataset; and for real deraining tasks, we cropped 3,000 paired patches from 784 images in the RealRain-1k-L training dataset. Each task was fine-tuned for 50k iterations. The results show that the performance of all methods was further improved, with significant gains on SIDD and RealRain-1k-L. Our method consistently maintained nearly the best performance.

2) *Generalization to unknown degradation type*: We utilize the All-in-One methods trained under the “**N+H+R+B+L**” setting and directly evaluate them on the training-unknown underwater and under-display-camera image restoration tasks. As shown in Tab. VII and Tab. VIII, our Perceive-IR significantly outperforms other general and All-in-One methods on these unknown tasks. These results demonstrate the superior generalization capability of Perceive-IR, particularly in handling unknown degradation scenarios.

3) *Generalization to unknown degradation severity*: We utilize the All-in-One methods trained under the noise levels of  $\sigma \in \{15, 25, 50\}$  to test on the unseen noise levels of  $\sigma \in \{60, 100\}$ . Tab. IX shows that our Perceive-IR outperforms other All-in-One methods on unknown noise level task, achieving PSNR scores of 27.11 (vs. 26.83 for Gridformer) on CBSD68 and 27.59 (vs. 27.24 for PromptIR) on Urban100 at  $\sigma = 60$ , and 20.67 (vs. 20.23 for PromptIR) on CBSD68 and 21.52 (vs. 21.52 for PromptIR) on Urban100 at  $\sigma = 100$ . These results demonstrate its superior generalization capability to handle unknown degradation severity.

TABLE VI

REAL-WORLD RESTORATION RESULTS IN **ALL-IN-ONE** (“**N+H+R**” AND “**N+H+R+B+L**”) SETTINGS WITH STATE-OF-THE-ART **TASK-SPECIFIC**, **GENERAL**, AND **ALL-IN-ONE** IMAGE RESTORATION METHODS.  $\dagger$  INDICATES METHOD HAS BEEN FINE-TUNED ON THE DATASET CORRESPONDING TO THE RESPECTIVE REAL-WORLD SCENES. DUE TO THE UNAVAILABILITY OF WEIGHTS FOR INSTRUCTIR-3D AND INSTRUCTIR-5D, WE UTILIZE THE RESULTS OF INSTRUCTIR-7D FOR EVALUATION.

Method	<b>N+H+R</b>			<b>N+H+R+B+L</b>		
	SIDD [68]	RTTS [52]	RealRain-1k-L [69]	SIDD [68]	RTTS [52]	RealRain-1k-L [69]
	PSNR $\uparrow$ /SSIM $\uparrow$	FADE $\downarrow$ /BRISQUE $\downarrow$ /NIMA $\uparrow$	PSNR $\uparrow$ /SSIM $\uparrow$ /LPIPS $\downarrow$	PSNR $\uparrow$ /SSIM $\uparrow$	FADE $\downarrow$ /BRISQUE $\downarrow$ /NIMA $\uparrow$	PSNR $\uparrow$ /SSIM $\uparrow$ /LPIPS $\downarrow$
Original	23.66/0.439	2.484/36.642/4.483	25.95/0.868/0.407	23.66/0.439	2.484/36.642/4.483	25.95/0.868/0.407
◇ ADFNet [3]	24.12/0.473 <sup>†</sup>	1.656/31.254/4.307	21.25/0.750/0.414	24.07/0.470 <sup>†</sup>	1.738/31.802/4.321	20.84/0.746/0.426
◇ DehazeFormer [6]	23.89/0.457	1.283/24.395/4.504	21.92/0.751/0.408	23.76/0.451	1.354/28.613/4.552	21.68/0.748/0.421
◇ DRSformer [9]	23.94/0.461	1.464/28.697/4.413	22.59/0.773/0.402	23.87/0.453	1.488/29.105/4.371	22.03/0.755/0.411
◇ FSNet [20]	24.26/0.470	1.452/30.681/4.325	22.61/0.760/0.404	24.33/0.468	1.560/32.964/4.139	21.96/0.754/0.408
◇ MambaIR [40]	24.19/0.465	1.326/25.432/4.421	22.34/0.754/0.410	23.87/0.457	1.494/27.313/4.313	21.69/0.751/0.417
◇ AirNet [23]	23.86/0.459	1.534/26.845/4.559	19.88/0.683/0.401	23.64/0.441	1.627/28.345/4.552	18.64/0.655/0.409
◇ AirNet <sup>†</sup> [23]	38.34/0.952	1.198/22.512/4.753	31.24/0.943/0.183	38.07/0.949	1.227/23.372/4.673	30.87/0.938/0.196
◇ PromptIR [27]	24.58/0.482	1.298/23.354/4.529	22.98/0.767/0.403	24.11/0.469	1.356/25.349/4.437	22.31/0.759/0.396
◇ PromptIR <sup>†</sup> [27]	38.73/0.954	<b>1.012/20.607/4.849</b>	31.69/0.946/0.167	38.66/ <b>0.954</b>	1.185/21.326/4.803	31.29/0.942/0.178
◇ InstructIR-7D [33]	24.35/0.479	1.257/20.549/4.573	27.21/0.901/0.373	24.35/0.479	1.257/20.549/4.573	27.21/0.901/0.373
◇ <b>Perceive-IR (Ours)</b>	24.88/0.504	1.213/21.621/4.681	27.79/0.915/0.354	24.65/0.491	1.278/23.523/4.624	27.43/0.903/0.370
◇ <b>Perceive-IR<sup>†</sup> (Ours)</b>	<b>39.04/0.954</b>	<b>1.097/18.345/4.901</b>	<b>32.05/0.951/0.144</b>	<b>38.92/0.952</b>	<b>1.185/19.021/4.872</b>	<b>31.61/0.948/0.160</b>

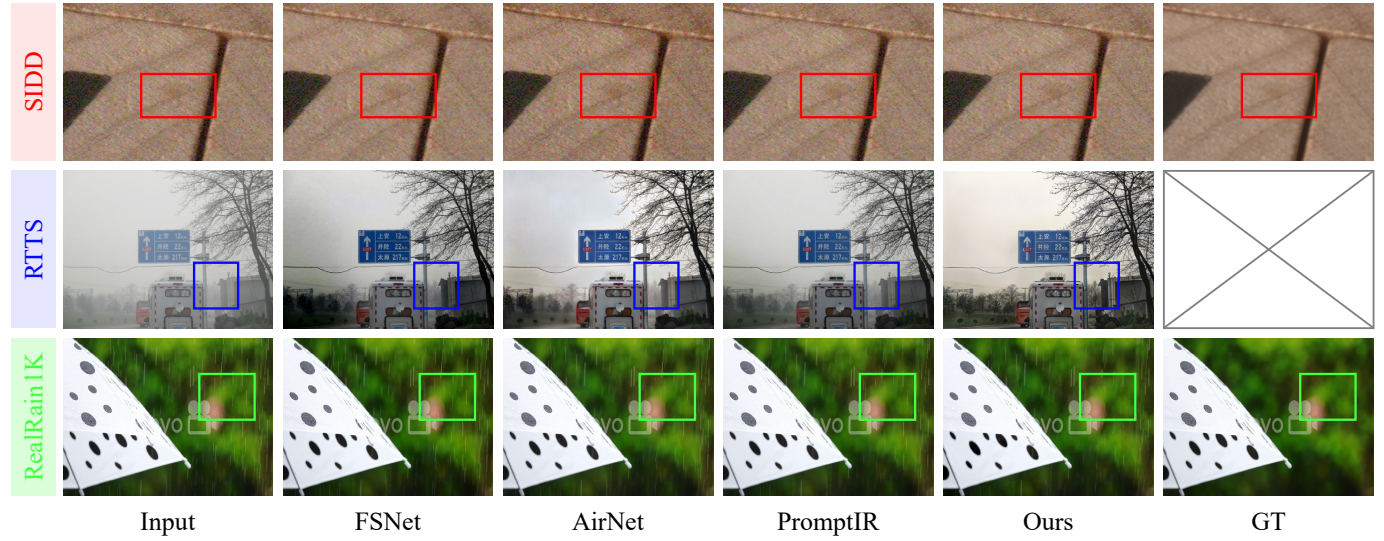


Fig. 9. Visual comparisons of Perceive-IR with state-of-the-art All-in-One methods under the “**N+H+R+B+L**” setting for zero-short generalization in real-world scenes. Zoom-in for best view.

TABLE VII

PERFORMANCE COMPARISONS ON TRAINING-UNSEEN UNDERWATER IMAGE RESTORATION TASK. WE USE THE ALL-IN-ONE METHODS (PRE-TRAINED UNDER “**N+H+R+B+L**” TRAINING SETTING) TO DIRECTLY TEST ON THE UIEB [70] DATASET. THE PROMPT USED IN INSTRUCTIR [33] IS “*This underwater image is poor, please enhance it.*”.

Method	<b>UIEB [70]</b>			<b>C60 [70]</b>	
	PSNR $\uparrow$	SSIM $\uparrow$	LPIPS $\downarrow$	UCIQE $\uparrow$	UIQM $\uparrow$
NAFNet [18]	18.34	0.763	0.365	0.480	1.984
Restormer [19]	18.69	0.782	0.336	0.497	2.135
AirNet [23]	18.96	0.797	0.283	0.505	2.114
PromptIR [27]	20.19	0.827	0.256	0.527	2.305
Gridformer [32]	20.48	0.846	0.243	0.540	2.517
InstructIR-7D [33]	21.07	0.872	0.189	0.552	2.489
<b>Perceive-IR</b>	<b>21.75</b>	<b>0.891</b>	<b>0.168</b>	<b>0.561</b>	<b>2.558</b>

TABLE VIII

PERFORMANCE COMPARISONS ON TRAINING-UNSEEN UNDER-DISPLAY CAMERA IMAGE RESTORATION TASK. WE USE THE ALL-IN-ONE METHODS (PRE-TRAINED UNDER “**N+H+R+B+L**” TRAINING SETTING) TO DIRECTLY TEST ON THE TOLED/POLED [71] DATASETS. THE PROMPT USED IN INSTRUCTIR [33] IS “*This under-display camera image is poor, please enhance it.*”.

Method	<b>TOLED [71]</b>			<b>POLED [71]</b>		
	PSNR $\uparrow$	SSIM $\uparrow$	LPIPS $\downarrow$	PSNR $\uparrow$	SSIM $\uparrow$	LPIPS $\downarrow$
NAFNet [18]	24.90	0.828	0.360	10.68	0.475	0.713
Restormer [19]	25.74	0.801	0.338	13.94	0.428	0.681
AirNet [23]	25.47	0.794	0.316	12.97	0.462	0.714
PromptIR [27]	27.23	0.811	0.319	14.54	<b>0.493</b>	0.728
Gridformer [32]	26.17	0.826	0.337	14.09	0.452	0.751
InstructIR-7D [33]	25.85	0.843	0.305	13.87	0.431	0.652
<b>Perceive-IR</b>	<b>29.17</b>	<b>0.875</b>	<b>0.294</b>	<b>15.89</b>	0.477	<b>0.531</b>

### E. Visual Results

Figs. 6-7 present the restoration results obtained by state-of-the-art All-in-One methods for both All-in-One (“**N+H+R**”)

TABLE IX  
PERFORMANCE COMPARISONS OF ALL-IN-ONE METHODS ON UNSEEN  
NOISE LEVEL OF  $\sigma = 60, 100$ .

Method	CBSD68 [49]		Urban100 [50]	
	$\sigma = 60$	$\sigma = 100$	$\sigma = 60$	$\sigma = 100$
AirNet [23]	26.01	14.29	25.11	14.23
PromptIR [27]	26.71	20.23	27.24	20.94
Gridformer [32]	26.83	20.14	27.16	20.85
<b>Perceive-IR</b>	<b>27.11</b>	<b>20.67</b>	<b>27.59</b>	<b>21.52</b>

TABLE X  
EFFECTIVENESS OF DIFFERENT COMPONENTS ON THE RAIN100L [53]  
DATASET.

Index	Prompt	DINO-v2	PGM	CFE	PSNR $\uparrow$	SSIM $\uparrow$
(a)	<b>X</b>	<b>X</b>	<b>X</b>	<b>X</b>	37.15	0.975
(b)	<b>✓</b>	<b>X</b>	<b>X</b>	<b>X</b>	37.37	0.979
(c)	<b>X</b>	<b>✓</b>	<b>X</b>	<b>X</b>	37.32	0.979
(d)	<b>X</b>	<b>X</b>	<b>✓</b>	<b>X</b>	37.28	0.978
(e)	<b>X</b>	<b>X</b>	<b>X</b>	<b>✓</b>	37.23	0.977
(f)	<b>✓</b>	<b>✓</b>	<b>X</b>	<b>X</b>	37.52	0.981
(g)	<b>X</b>	<b>X</b>	<b>✓</b>	<b>✓</b>	37.38	0.979
(h)	<b>X</b>	<b>✓</b>	<b>✓</b>	<b>✓</b>	37.45	0.979
(i)	<b>✓</b>	<b>X</b>	<b>✓</b>	<b>✓</b>	37.50	0.980
(j)	<b>✓</b>	<b>✓</b>	<b>✓</b>	<b>✓</b>	<b>37.76</b>	<b>0.982</b>

and One-by-One setting. In noisy scenarios, Perceive-IR produces clear and sharp denoised outputs, preserving fine textures compared to AirNet [23], PromptIR [27], and InstructIR [33] (e.g., the head and stomach texture parts in rows 1 and 2 of Fig. 6). In challenging hazy scenes, as seen in row 3, AirNet and PromptIR generate results with low color fidelity, while InstructIR produces blurrier results. In row 4, these comparison methods generate results with additional offsets. Conversely, the results generated by our method maintain good color and structural integrity. In deraining task, as shown in the iron-frame region in row 6, AirNet, PromptIR, and InstructIR introduce additional artifacts. In contrast, our approach produced more realistic results. The same trend is illustrated in Fig. 7. These findings demonstrate the effectiveness of our method. Furthermore, as illustrated in Fig. 9, although all methods struggle in zero-shot real-world scenarios, our approach still achieves superior visual results. These results underscore the remarkable zero-shot generalization capability of Perceive-IR for real-world image restoration, achieving state-of-the-art performance across a wide range of unknown degradation scenarios.

TABLE XI  
EFFECTIVENESS OF THE DIFFERENT LOSS FUNCTIONS ON THE RAIN100L  
[53] DATASET.

Index	$\mathcal{L}_{clip}$	$\mathcal{L}_{dpl}$	$\mathcal{L}_{cl}$	PSNR $\uparrow$	SSIM $\uparrow$
(a)	<b>X</b>	<b>X</b>	<b>X</b>	37.30	0.978
(b)	<b>✓</b>	<b>X</b>	<b>X</b>	37.51	0.980
(c)	<b>X</b>	<b>✓</b>	<b>X</b>	37.42	0.979
(d)	<b>X</b>	<b>X</b>	<b>✓</b>	37.37	0.979
(e)	<b>X</b>	<b>✓</b>	<b>✓</b>	37.46	0.979
(f)	<b>✓</b>	<b>✓</b>	<b>X</b>	37.61	0.981
(g)	<b>✓</b>	<b>X</b>	<b>✓</b>	37.55	0.981
(h)	<b>✓</b>	<b>✓</b>	<b>✓</b>	<b>37.76</b>	<b>0.982</b>

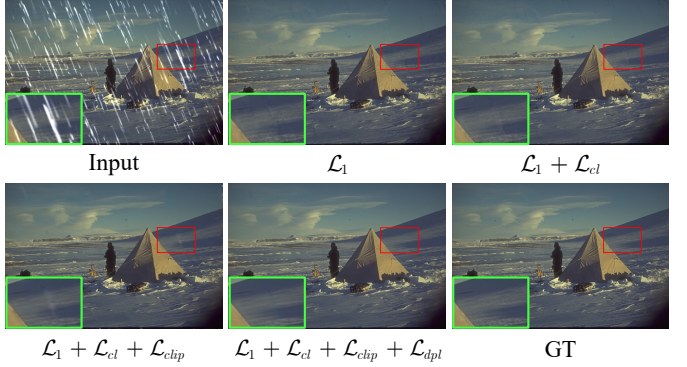


Fig. 10. Visual comparison of the restored images obtained using the individual loss schemes and the proposed scheme.

#### F. Ablation Study

We conduct several ablation experiments to demonstrate the effectiveness of each component in the proposed Perceive-IR. All ablation experiments are performed on the image deraining task (Rain100L [53]) by training models for 100K iterations except for special instructions.

1) *Effects of Different Components*: As shown in Tab. X, we evaluate the effectiveness of various components through a comparison with the baseline method (index a) that excludes our modules. The baseline adopts Restormer [19] as its backbone. ‘Prompt’ denotes the prompt learning stage. The settings are as follows: (1) ‘w/o Prompt’ indicates the removal of prompt learning, where the cross-entropy loss ( $\mathcal{L}_{ce}$ ) is omitted; (2) ‘w/o DINO-v2’ refers to replacing the semantic prior  $\mathbf{F}_l$  with learnable parameters; (3) ‘w/o PGM’ denotes the direct application of cross-attention using  $\mathbf{F}_l$ ’s features without the processing through  $\mathbf{Z}$  and  $\mathbf{F}_l$ ; and (4) ‘w/o CFE’ corresponds to the substitution of  $\mathbf{Z}$  with learnable parameters.

Specifically, without prompt learning and DINO-v2 (index g), the average PSNR performance is reduced by 0.38 dB. Similarly, without PGM and CFE (index f), the performance is reduced by 0.24 dB. When compared to other modules, the improvement brought by prompt learning is more significant, as shown in (indexes b-e). This suggests that the proposed CLIP-based prompt learning strategy is crucial to the performance. Overall, our model (index j) achieves a significant average PSNR improvement of 0.61 dB over the baseline, which is attributed to the effectiveness of each proposed component.

2) *Effects of Different Loss Functions*: As shown in Tab. XI, we determine the effectiveness of Perceive-IR under different loss functions. The baseline (index a) uses only pixel-level reconstruction loss  $\mathcal{L}_{rec}$ . Specifically, compared to the baseline, the approach incorporating  $\mathcal{L}_{clip}$ ,  $\mathcal{L}_{dpl}$ , and  $\mathcal{L}_{cl}$  simultaneously achieves a PSNR improvement of 0.46 dB. Furthermore, by integrating the perceptual capabilities of CLIP, the utilization of  $\mathcal{L}_{clip}$  (index b) results in a PSNR improvement of 0.09 dB and 0.14 dB, respectively, over the use of  $\mathcal{L}_{dpl}$  (index c) and  $\mathcal{L}_{cl}$  (index d) alone. These findings demonstrate that combining multiple loss functions and leveraging CLIP’s perceptual properties can significantly elevate the quality of image restoration. Fig. 10 illustrates the visual results of various schemes using individual loss modules and our proposed scheme. As the proposed loss modules are

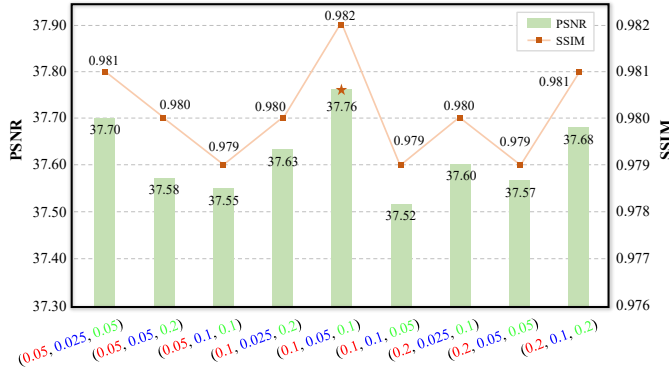


Fig. 11. Comparison of PSNR and SSIM with different weight between different loss function on the Rain100L [53] dataset. red, blue, and green are the weights  $\lambda_1$ ,  $\lambda_2$ , and  $\lambda_3$  in Eq. 13, respectively.

successively added, the restored image more closely resembles the ground truth.

In addition, we further explored the effect of weights between different loss functions. As shown in Fig. 11, peak performance is observed at  $(\lambda_1, \lambda_2, \lambda_3) = (0.1, 0.05, 0.1)$ . Similarly, sub-optimal performance is obtained when  $\lambda_1$  and  $\lambda_3$  are larger than  $\lambda_2$ , e.g.,  $(0.05, 0.025, 0.05)$  and  $(0.2, 0.1, 0.2)$ . In other cases, the performance degradation is more significant. Thus, in our method,  $\lambda_1$ ,  $\lambda_2$ , and  $\lambda_3$  are set as  $0.1$ ,  $0.05$ , and  $0.1$ , respectively.

3) *Effects of Prompt Number and Initialization Schemes:* In this study, we examine the impacts of different number of prompts and prompt initialization settings. We consider three scenarios: two, three, and four pairs of prompt-image pairs. Specifically, we explore three configurations for prompt initialization, **i)** Fixed: The prompts are fixed throughout the entire training process. **ii)** Random initialization: The prompts are initially randomized and then learned from there. **iii)** Partial random initialization: Part of the token is initialized randomly while one token is fixed as a specific word. For example, a five-token prompt is initialized as “ $\times, \times, \times, \times, \text{excellent}$ ”, where “ $\times$ ” denotes random initialization. And the entire prompt is updated during prompt learning.

As shown in Table XII, using three prompts in the CLIP model, with the same initialization strategy, outperforms using two or four prompts. The use of two prompt-image pairs may result in inadequate model discrimination, while four pairs could offer too much detail, negatively affecting the portrayal of image quality. This suggests that an appropriate number of prompts is beneficial in providing a more precise guide for the restoration process.

In all prompt configurations, “Partial random initialization” consistently outperforms both “Fixed” and “Random initialization”. The use of fixed or random prompts can lead to performance degradation due to the domain gap between the pre-training data of the CLIP model and the specifics of our task. Random prompts slightly enhance performance by easing learning constraints compared with fixed prompts. Therefore, the partial random initialization strategy achieves optimal results, likely because it provides more effective guidance and ensures ample learning space across various prompt scenarios. We additionally consider the formulation of the specified

words. As seen in (indexes g, i) and (indexes l, m), such vague definitions are prone to appear in the data of the pre-trained model, which reduces the performance. When the prompt and image quality do not align, as in (indexes h, i), it disrupts the prompt learning stage, leading to a significant drop in performance. In all, our scheme (index i) achieves the best results and proves its superiority.

4) *Effects of Different Combinations of Degradation:* In this study, we assess the performance of Perceive-IR under various combinations of degradation types. As demonstrated in Tab. XIII, the performance of the model is optimal on a single task. With the number of tasks increasing, the performance of each task oscillates below the optimal value. In addition, there may be some interesting phenomena under different combinations of degradation. For example, models trained in the “N+H+L” setting show superior performance in denoising and dehazing compared to those trained in the “N+H+B” setting. Similarly, models trained in the “N+H+R+L” setting have better performance on denoising and dehazing than models trained in the “N+H+R+B” setting, but worse performance on the deraining task. This may be because the distribution of low-light images may contain more noise and haze-like artifacts, which can enhance the model’s ability to handle these types of degradation. On the other hand, deraining requires specific features related to rain streaks, which might not be as prevalent in low-light conditions.

5) *Effects of Restoration Models for Prompt Learning:* In this part, we examine the impact of restoration methods on prompt learning. As shown in Tab. XIV, advanced All-in-One models like PromptIR [27] underperform AirNet [23], while general models like Restormer [19] surpass MPRNet [16]. This can be explained by two factors. First, PromptIR’s high-quality outputs exceed the “mediocre” standard, causing ambiguity in prompt learning. Second, such high-quality restorations may cause the “mediocre” prompt to converge towards “excellent”, reducing the distinctiveness of the three prompts to essentially two. In contrast, MPRNet’s lower-quality results show the opposite effect. Overall, “medium” quality restorations from appropriate methods are more effective for prompt learning.

## G. Discussion and Limitation

To validate the adaptability of our method for different restoration backbones, we conducted extensive experiments using NAFNet [18], Restormer [19], X-Restormer [74], and GRL [72] as the backbones in the restoration stage. As demonstrated in Tab. XV, the proposed framework exhibits strong compatibility and superior performance across various architectures. Specifically, Perceive-IR<sub>NAFNet-128</sub> achieves 32.52/29.71 dB PSNR under “N+H+R” and “N+H+R+B+L” settings, surpassing PromptIR [27] by 0.46/0.56 dB and InstructIR [33] by 0.09/0.16 dB. Notably, our X-Restormer-128 variant attains state-of-the-art 32.66/29.92 dB PSNR with a 5.6% parameter reduction compared to the original Restormer backbone (39.67M vs. 42.02M). Consistent performance gains are observed in the GRL-128 variant (*i.e.*, +0.28 dB over the base NAFNet-128, +0.24 dB over the base Restormer-128, and +0.16 dB over the base X-Restormer-128). When trained

TABLE XII

PERFORMANCE COMPARISONS ON THE RAIN100L [53] DATASET AMONG DIFFERENT PROMPT INITIALIZATION SETTINGS FOR THE CLIP MODEL.

Type	Index	Prompt Setting	PSNR↑	SSIM↑
Two pairs of prompt-image	(a)	Fixed (“excellent”/“terrible”)	37.36	0.979
	(b)	Random initialization	37.49	0.980
	(c)	Partial random initialization (“excellent”/“terrible”)	37.56	0.981
Three pairs of prompt-image	(d)	Fixed (“excellent”/“mediocre”/“terrible”)	37.45	0.979
	(e)	Fixed (“good”/“moderate”/“bad”)	37.50	0.980
	(f)	Random initialization	37.52	0.981
	(g)	Partial random initialization (“good”/“moderate”/“bad”)	37.68	0.982
	(h)	Partial random initialization (“terrible”/“moderate”/“excellent”)	37.43	0.979
	(i)	Partial random initialization (“excellent”/“mediocre”/“terrible”) (Ours)	<b>37.76</b>	<b>0.982</b>
Four pairs of prompt-image	(j)	Fixed (“excellent”/“slightly better”/“slightly worse”/“terrible”)	37.44	0.979
	(k)	Random initialization	37.56	0.981
	(l)	Partial random initialization (“excellent”/“good”/“bad”/“terrible”)	37.63	0.982
	(m)	Partial random initialization (“excellent”/“slightly better”/“slightly worse”/“terrible”)	37.67	0.982

TABLE XIII

PERFORMANCE OF THE PROPOSED PERCEIVE-IR, WHEN CONDUCTED ON VARIOUS COMBINATIONS OF DEGRADATION TYPES. NUMBER OF COMBINATIONS OF TASKS FROM 1 TO 5.

Degradation					Denoising (CBSD68 [49])			Dehazing	Deraining	Deblurring	Low-Light
N	H	R	B	L	$\sigma = 15$	$\sigma = 25$	$\sigma = 50$	SOTS [52]	Rain100L [53]	GoPro [11]	LOL [13]
✓	✗	✗	✗	✗	34.38/0.939	31.74/0.898	28.53/0.813	-	-	-	-
✗	✓	✗	✗	✗	-	-	-	31.65/0.977	-	-	-
✗	✗	✓	✗	✗	-	-	-	-	38.41/0.984	-	-
✗	✗	✗	✓	✗	-	-	-	-	-	32.83/0.960	-
✗	✗	✗	✗	✓	-	-	-	-	-	-	23.24/0.838
✓	✓	✗	✗	✗	34.35/0.939	31.70/0.897	28.46/0.812	30.79/0.975	-	-	-
✓	✗	✓	✗	✗	34.31/0.937	31.66/0.895	28.41/0.810	-	38.11/0.980	-	-
✗	✓	✓	✗	✗	-	-	-	30.92/0.976	38.23/0.981	-	-
✗	✗	✗	✓	✓	-	-	-	-	-	32.33/0.953	22.97/0.835
✓	✓	✓	✗	✗	34.13/0.934	31.53/0.890	28.31/0.804	30.87/0.975	38.29/0.980	-	-
✓	✓	✗	✓	✗	34.16/0.934	31.55/0.890	28.32/0.803	30.11/0.972	-	31.29/0.934	-
✓	✓	✓	✗	✓	34.20/0.935	31.57/0.891	28.33/0.804	30.36/0.973	-	-	22.90/0.834
✓	✓	✓	✓	✗	34.11/0.932	31.50/0.888	28.26/0.802	28.87/0.967	37.83/0.979	30.31/0.911	-
✓	✓	✓	✓	✓	34.13/0.933	31.52/0.889	28.27/0.802	29.62/0.970	37.49/0.978	-	22.76/0.831
✓	✓	✓	✗	✓	34.10/0.932	31.48/0.888	28.25/0.801	29.23/0.968	-	29.89/0.897	22.81/0.834
✓	✓	✓	✓	✓	34.04/0.931	31.44/0.887	28.19/0.801	28.19/0.964	37.25/0.977	29.46/0.886	22.88/0.833

TABLE XIV

PERFORMANCE COMPARISONS ON THE RAIN100L [53] DATASET AMONG DIFFERENT RESTORATION MODELS FOR THE PROMPT LEARNING STAGE.

Method	PSNR↑	SSIM↑
Perceive-IR (MPRNet [16])	37.68	0.982
Perceive-IR (AirNet [23])	37.64	0.981
Perceive-IR (PromptIR [27])	37.57	0.981
Perceive-IR (Restormer [19]) (Ours)	<b>37.76</b>	<b>0.982</b>

with a patch size of 256, the performance of all methods improves further, with the relative performance advantages across different backbones remaining intact. These results confirm that our approach serves as a plug-and-play module while enabling scalable integration with advanced models, where the decoupled design allows future works to directly inherit our innovations through backbone upgrades without structural modifications.

Although our Perceive-IR has achieved superior generaliza-

TABLE XV  
PERFORMANCE COMPARISONS OF PERCEIVE-IR WITH DIFFERENT RESTORATION BACKBONES UNDER THE “N+H+R” AND “N+H+R+B+L” TRAINING SETTINGS VERSUS STATE-OF-THE-ART ALL-IN-ONE IMAGE RESTORATION METHODS. (128, 256) INDICATES PATCH SIZE.

Method	N+H+R		N+H+R+B+L		Params (M)
	PSNR↑	SSIM↑	PSNR↑	SSIM↑	
AirNet [23]	31.20	0.910	25.49	0.846	8.93
PromptIR [27]	32.06	0.913	29.15	0.904	32.96
InstructIR [33]	32.43	0.913	29.55	0.907	15.84
Perceive-IR <sub>NAFNet-128</sub>	32.52	0.915	29.71	0.908	21.73
Perceive-IR <sub>NAFNet-256</sub>	32.59	0.916	29.82	0.908	21.73
Perceive-IR <sub>Restormer-128</sub>	32.63	0.917	29.84	0.909	42.02
Perceive-IR <sub>Restormer-256</sub>	32.67	0.917	29.95	0.910	42.02
Perceive-IR <sub>X-Restormer-128</sub>	32.66	0.917	29.92	0.909	39.67
Perceive-IR <sub>X-Restormer-256</sub>	32.71	0.918	30.04	0.910	39.67
Perceive-IR <sub>GRL-128</sub>	32.68	0.917	29.99	0.910	35.48
Perceive-IR <sub>GRL-256</sub>	<b>32.72</b>	<b>0.918</b>	<b>30.08</b>	<b>0.911</b>	35.48

tion ability and scalability in addressing multiple degradations, its flexibility in blind real-world conditions may be limited. Moreover, while Perceive-IR demonstrates superiority over the state-of-the-art All-in-One and general image restoration methods, it still falls short when compared to the most advanced state-of-the-art task-specific methods, particularly in tasks such as deblurring and low-light enhancement. Lastly, the interrelationships among the various degradation are not sufficiently clear, for example, as shown in Tab. XIII, the model performs better on the dehazing task in the “N+H+R+B” setting compared to the “N+H+R+L” setting, yet the deraining performance is degraded.

## V. CONCLUSION

This paper proposes Perceive-IR, a novel backbone-agnostic framework for All-in-One image restoration that achieves fine-grained quality control through a two-stage process. First, a multi-level quality-driven prompt learning stage trains a quality perceiver to distinguish three-tier quality levels by optimizing prompt-image alignment in the CLIP space. Second, a restoration stage integrates the perceiver with a difficulty-adaptive perceptual loss for quality-aware learning. Additionally, we introduce a Semantic Guidance Module and Compact Feature Extraction to enhance restoration by leveraging semantic priors and degradation-specific features. Extensive experiments demonstrate that Perceive-IR outperforms state-of-the-art methods, generalizes to real-world degradation scenarios, and adapts seamlessly to various backbone networks, highlighting its robustness and flexibility.

## REFERENCES

- [1] K. Zhang, W. Zuo, Y. Chen, D. Meng, and L. Zhang, “Beyond a gaussian denoiser: Residual learning of deep cnn for image denoising,” *IEEE Trans. Image Process.*, vol. 26, no. 7, pp. 3142–3155, 2017.
- [2] K. Zhang, W. Zuo, and L. Zhang, “Ffdnet: Toward a fast and flexible solution for cnn-based image denoising,” *IEEE Trans. Image Process.*, vol. 27, no. 9, pp. 4608–4622, 2018.
- [3] H. Shen, Z.-Q. Zhao, and W. Zhang, “Adaptive dynamic filtering network for image denoising,” in *Proc. AAAI Conf. Artif. Intell. (AAAI)*, vol. 37, no. 2, 2023, pp. 2227–2235.
- [4] B. Cai, X. Xu, K. Jia, C. Qing, and D. Tao, “Dehazenet: An end-to-end system for single image haze removal,” *IEEE Trans. Image Process.*, vol. 25, no. 11, pp. 5187–5198, 2016.
- [5] Y. Dong, Y. Liu, H. Zhang, S. Chen, and Y. Qiao, “Fd-gan: Generative adversarial networks with fusion-discriminator for single image dehazing,” in *Proc. AAAI Conf. Artif. Intell. (AAAI)*, vol. 34, no. 07, 2020, pp. 10 729–10 736.
- [6] Y. Song, Z. He, H. Qian, and X. Du, “Vision transformers for single image dehazing,” *IEEE Trans. Image Process.*, vol. 32, pp. 1927–1941, 2023.
- [7] R. Yasarla and V. M. Patel, “Uncertainty guided multi-scale residual learning-using a cycle spinning cnn for single image de-raining,” in *Proc. IEEE/CVF Conf. Comput. Vis. Pattern Recognit. (CVPR)*, 2019, pp. 8405–8414.
- [8] K. Jiang, Z. Wang, P. Yi, C. Chen, B. Huang, Y. Luo, J. Ma, and J. Jiang, “Multi-scale progressive fusion network for single image deraining,” in *Proc. IEEE/CVF Conf. Comput. Vis. Pattern Recognit. (CVPR)*, 2020, pp. 8346–8355.
- [9] X. Chen, H. Li, M. Li, and J. Pan, “Learning a sparse transformer network for effective image deraining,” in *Proc. IEEE/CVF Conf. Comput. Vis. Pattern Recognit. (CVPR)*, June 2023, pp. 5896–5905.
- [10] O. Kupyn, V. Budzan, M. Mykhailych, D. Mishkin, and J. Matas, “Deblurgan: Blind motion deblurring using conditional adversarial networks,” in *Proc. IEEE/CVF Conf. Comput. Vis. Pattern Recognit. (CVPR)*, 2018, pp. 8183–8192.
- [11] S. Nah, T. Hyun Kim, and K. Mu Lee, “Deep multi-scale convolutional neural network for dynamic scene deblurring,” in *Proc. IEEE/CVF Conf. Comput. Vis. Pattern Recognit. (CVPR)*, 2017, pp. 3883–3891.
- [12] F.-J. Tsai, Y.-T. Peng, Y.-Y. Lin, C.-C. Tsai, and C.-W. Lin, “Stripformer: Strip transformer for fast image deblurring,” in *Proc. Eur. Conf. Comput. Vis. (ECCV)*, 2022, pp. 146–162.
- [13] C. Wei, W. Wang, W. Yang, and J. Liu, “Deep retinex decomposition for low-light enhancement,” in *Proc. Brit. Mach. Vis. Conf. (BMVC)*, 2018.
- [14] W. Wu, J. Weng, P. Zhang, X. Wang, W. Yang, and J. Jiang, “Uretinexnet: Retinex-based deep unfolding network for low-light image enhancement,” in *Proc. IEEE/CVF Conf. Comput. Vis. Pattern Recognit. (CVPR)*, 2022, pp. 5901–5910.
- [15] Y. Cai, H. Bian, J. Lin, H. Wang, R. Timofte, and Y. Zhang, “Retinexformer: One-stage retinex-based transformer for low-light image enhancement,” in *Proc. IEEE/CVF Int. Conf. Comput. Vis. (ICCV)*, 2023, pp. 12 504–12 513.
- [16] S. W. Zamir, A. Arora, S. Khan, M. Hayat, F. S. Khan, M.-H. Yang, and L. Shao, “Multi-stage progressive image restoration,” in *Proc. IEEE/CVF Conf. Comput. Vis. Pattern Recognit. (CVPR)*, 2021, pp. 14 816–14 826.
- [17] S. W. Zamir, A. Arora, S. Khan, M. Hayat, F. S. Khan, M.-H. Yang, and L. Shao, “Learning enriched features for fast image restoration and enhancement,” *IEEE Trans. Pattern Anal. Mach. Intell.*, vol. 45, no. 2, pp. 1934–1948, 2022.
- [18] L. Chen, X. Chu, X. Zhang, and J. Sun, “Simple baselines for image restoration,” in *Proc. Eur. Conf. Comput. Vis. (ECCV)*, 2022, pp. 17–33.
- [19] S. W. Zamir, A. Arora, S. Khan, M. Hayat, F. S. Khan, and M.-H. Yang, “Restormer: Efficient transformer for high-resolution image restoration,” in *Proc. IEEE/CVF Conf. Comput. Vis. Pattern Recognit. (CVPR)*, 2022, pp. 5728–5739.
- [20] Y. Cui, W. Ren, X. Cao, and A. Knoll, “Image restoration via frequency selection,” *IEEE Trans. Pattern Anal. Mach. Intell.*, vol. 46, no. 2, pp. 1093–1108, 2023.
- [21] B. Xia, Y. Zhang, S. Wang, Y. Wang, X. Wu, Y. Tian, W. Yang, and L. Van Gool, “Diffir: Efficient diffusion model for image restoration,” in *Proc. IEEE/CVF Int. Conf. Comput. Vis. (ICCV)*, 2023, pp. 13 095–13 105.
- [22] L. Liu, L. Xie, X. Zhang, S. Yuan, X. Chen, W. Zhou, H. Li, and Q. Tian, “Tape: Task-agnostic prior embedding for image restoration,” in *Proc. Eur. Conf. Comput. Vis. (ECCV)*, 2022, pp. 447–464.
- [23] B. Li, X. Liu, P. Hu, Z. Wu, J. Lv, and X. Peng, “All-in-one image restoration for unknown corruption,” in *Proc. IEEE/CVF Conf. Comput. Vis. Pattern Recognit. (CVPR)*, 2022, pp. 17 452–17 462.
- [24] Z. Tan, Y. Wu, Q. Liu, Q. Chu, L. Lu, J. Ye, and N. Yu, “Exploring the application of large-scale pre-trained models on adverse weather removal,” *IEEE Trans. Image Process.*, vol. 33, pp. 1683–1698, 2024.
- [25] J. Zhang, J. Huang, M. Yao, Z. Yang, H. Yu, M. Zhou, and F. Zhao, “Ingredient-oriented multi-degradation learning for image restoration,” in *Proc. IEEE/CVF Conf. Comput. Vis. Pattern Recognit. (CVPR)*, 2023, pp. 5825–5835.
- [26] J. Ma, T. Cheng, G. Wang, Q. Zhang, X. Wang, and L. Zhang, “Prores: Exploring degradation-aware visual prompt for universal image restoration,” *arXiv preprint arXiv:2306.13653*, 2023.
- [27] V. Potlapalli, S. W. Zamir, S. Khan, and F. S. Khan, “Promptpir: Prompting for all-in-one blind image restoration,” in *Proc. Adv. Neural Inf. Process. Syst. (NeurIPS)*, 2023, pp. 71 275–71 293.
- [28] M. Yao, R. Xu, Y. Guan, J. Huang, and Z. Xiong, “Neural degradation representation learning for all-in-one image restoration,” *IEEE Trans. Image Process.*, vol. 33, pp. 5408–5423, 2024.
- [29] X. Lin, C. Ren, K. C. Chan, L. Qi, J. Pan, and M.-H. Yang, “Multi-task image restoration guided by robust dino features,” *arXiv preprint arXiv:2312.01677*, 2023.
- [30] Y.-W. Chen and S.-C. Pei, “Always clear days: Degradation type and severity aware all-in-one adverse weather removal,” *arXiv preprint arXiv:2310.18293*, 2023.
- [31] Z. Luo, F. K. Gustafsson, Z. Zhao, J. Sjölund, and T. B. Schön, “Controlling vision-language models for universal image restoration,” *arXiv preprint arXiv:2310.01018*, 2023.
- [32] T. Wang, K. Zhang, Z. Shao, W. Luo, B. Stenger, T. Lu, T.-K. Kim, W. Liu, and H. Li, “Gridformer: Residual dense transformer with grid structure for image restoration in adverse weather conditions,” *Int. J. Comput. Vis.*, vol. 132, no. 10, pp. 4541–4563, 2024.
- [33] M. V. Conde, G. Geigle, and R. Timofte, “High-quality image restoration following human instructions,” in *Proc. Eur. Conf. Comput. Vis. (ECCV)*, 2024, pp. 1–21.
- [34] A. Radford, J. W. Kim, C. Hallacy, A. Ramesh, G. Goh, S. Agarwal, G. Sastry, A. Askell, P. Mishkin, J. Clark *et al.*, “Learning transferable

visual models from natural language supervision,” in *Proc. Int. Conf. Mach. Learn. (ICML)*, 2021, pp. 8748–8763.

[35] M. Caron, H. Touvron, I. Misra, H. Jégou, J. Mairal, P. Bojanowski, and A. Joulin, “Emerging properties in self-supervised vision transformers,” in *Proc. IEEE/CVF Int. Conf. Comput. Vis. (ICCV)*, 2021, pp. 9650–9660.

[36] X. Zhang, N. Cai, H. Zhang, Y. Zhang, J. Di, and W. Lin, “Afd-former: A hybrid transformer with asymmetric flow division for synthesized view quality enhancement,” *IEEE Trans. Circuits Syst. Video Technol.*, vol. 33, no. 8, pp. 3786–3798, 2023.

[37] Y. Xiao, Q. Yuan, K. Jiang, X. Jin, J. He, L. Zhang, and C.-W. Lin, “Local-global temporal difference learning for satellite video super-resolution,” *IEEE Trans. Circuits Syst. Video Technol.*, vol. 34, no. 4, pp. 2789–2802, 2023.

[38] H. Ma, H. Li, C. Cheng, Z. Zhang, X. Song, and X.-J. Wu, “Learning a unified degradation-aware representation model for multi-modal image fusion,” *arXiv preprint arXiv:2503.07033*, 2025.

[39] C. Mou, Q. Wang, and J. Zhang, “Deep generalized unfolding networks for image restoration,” in *Proc. IEEE/CVF Conf. Comput. Vis. Pattern Recognit. (CVPR)*, 2022, pp. 17399–17410.

[40] H. Guo, J. Li, T. Dai, Z. Ouyang, X. Ren, and S.-T. Xia, “Mambair: A simple baseline for image restoration with state-space model,” in *Proc. Eur. Conf. Comput. Vis. (ECCV)*, 2024, pp. 222–241.

[41] T. Brown, B. Mann, N. Ryder, M. Subbiah, J. D. Kaplan, P. Dhariwal, A. Neelakantan, P. Shyam, G. Sastry, A. Askell *et al.*, “Language models are few-shot learners,” in *Proc. Adv. Neural Inf. Process. Syst. (NeurIPS)*, 2020, pp. 1877–1901.

[42] M. Jia, L. Tang, B.-C. Chen, C. Cardie, S. Belongie, B. Hariharan, and S.-N. Lim, “Visual prompt tuning,” in *Proc. Eur. Conf. Comput. Vis. (ECCV)*, 2022, pp. 709–727.

[43] Z. Liang, C. Li, S. Zhou, R. Feng, and C. C. Loy, “Iterative prompt learning for unsupervised backlit image enhancement,” in *Proc. IEEE/CVF Int. Conf. Comput. Vis. (ICCV)*, 2023, pp. 8094–8103.

[44] M. Oquab, T. Dariset, T. Moutakanni, H. Vo, M. Szafraniec, V. Khalidov, P. Fernandez, D. Haziza, F. Massa, A. El-Nouby *et al.*, “Dinov2: Learning robust visual features without supervision,” *arXiv preprint arXiv:2304.07193*, 2023.

[45] H. Wu, Y. Qu, S. Lin, J. Zhou, R. Qiao, Z. Zhang, Y. Xie, and L. Ma, “Contrastive learning for compact single image dehazing,” in *Proc. IEEE/CVF Conf. Comput. Vis. Pattern Recognit. (CVPR)*, 2021, pp. 10551–10560.

[46] Y. Zheng, J. Zhan, S. He, J. Dong, and Y. Du, “Curricular contrastive regularization for physics-aware single image dehazing,” in *Proc. IEEE/CVF Conf. Comput. Vis. Pattern Recognit. (CVPR)*, 2023, pp. 5785–5794.

[47] P. Arbelaez, M. Maire, C. Fowlkes, and J. Malik, “Contour detection and hierarchical image segmentation,” *IEEE Trans. Pattern Anal. Mach. Intell.*, vol. 33, no. 5, pp. 898–916, 2010.

[48] K. Ma, Z. Duanmu, Q. Wu, Z. Wang, H. Yong, H. Li, and L. Zhang, “Waterloo exploration database: New challenges for image quality assessment models,” *IEEE Trans. Image Process.*, vol. 26, no. 2, pp. 1004–1016, 2016.

[49] D. Martin, C. Fowlkes, D. Tal, and J. Malik, “A database of human segmented natural images and its application to evaluating segmentation algorithms and measuring ecological statistics,” in *Proc. IEEE/CVF Int. Conf. Comput. Vis. (ICCV)*, vol. 2, 2001, pp. 416–423.

[50] J.-B. Huang, A. Singh, and N. Ahuja, “Single image super-resolution from transformed self-exemplars,” in *Proc. IEEE/CVF Conf. Comput. Vis. Pattern Recognit. (CVPR)*, 2015, pp. 5197–5206.

[51] R. Franzen, “Kodak lossless true color image suite,” 1999, [Online]. Available: <http://r0k.us/graphics/kodak/>. [Accessed: Oct. 24, 2021].

[52] B. Li, W. Ren, D. Fu, D. Tao, D. Feng, W. Zeng, and Z. Wang, “Benchmarking single-image dehazing and beyond,” *IEEE Trans. Image Process.*, vol. 28, no. 1, pp. 492–505, 2018.

[53] W. Yang, R. T. Tan, J. Feng, J. Liu, Z. Guo, and S. Yan, “Deep joint rain detection and removal from a single image,” in *Proc. IEEE/CVF Conf. Comput. Vis. Pattern Recognit. (CVPR)*, 2017, pp. 1357–1366.

[54] R. Zhang, P. Isola, A. A. Efros, E. Shechtman, and O. Wang, “The unreasonable effectiveness of deep features as a perceptual metric,” in *Proc. IEEE/CVF Conf. Comput. Vis. Pattern Recognit. (CVPR)*, 2018, pp. 586–595.

[55] M. Yang and A. Sowmya, “An underwater color image quality evaluation metric,” *IEEE Trans. Image Process.*, vol. 24, no. 12, pp. 6062–6071, 2015.

[56] K. Panetta, C. Gao, and S. Agaian, “Human-visual-system-inspired underwater image quality measures,” *IEEE J. Oceanic Eng.*, vol. 41, no. 3, pp. 541–551, 2015.

[57] J. Ke, Q. Wang, Y. Wang, P. Milanfar, and F. Yang, “Musiq: Multi-scale image quality transformer,” in *Proc. IEEE/CVF Int. Conf. Comput. Vis. (ICCV)*, 2021, pp. 5148–5157.

[58] L. K. Choi, J. You, and A. C. Bovik, “Referenceless prediction of perceptual fog density and perceptual image defogging,” *IEEE Trans. Image Process.*, vol. 24, no. 11, pp. 3888–3901, 2015.

[59] A. Mittal, A. K. Moorthy, and A. C. Bovik, “Blind/referenceless image spatial quality evaluator,” in *Proc. Asilomar Conf. Signals, Syst., Comput. (ASILOMAR)*, 2011, pp. 723–727.

[60] H. Talebi and P. Milanfar, “Nima: Neural image assessment,” *IEEE Trans. Image Process.*, vol. 27, no. 8, pp. 3998–4011, 2018.

[61] H. Gao, X. Tao, X. Shen, and J. Jia, “Dynamic scene deblurring with parameter selective sharing and nested skip connections,” in *Proc. IEEE/CVF Conf. Comput. Vis. Pattern Recognit. (CVPR)*, 2019, pp. 3848–3856.

[62] Q. Fan, D. Chen, L. Yuan, G. Hua, N. Yu, and B. Chen, “A general decoupled learning framework for parameterized image operators,” *IEEE Trans. Pattern Anal. Mach. Intell.*, vol. 43, no. 1, pp. 33–47, 2019.

[63] Z. Chen, Y. Zhang, D. Liu, B. Xia, J. Gu, L. Kong, and X. Yuan, “Hierarchical integration diffusion model for realistic image deblurring,” in *Proc. Adv. Neural Inf. Process. Syst. (NeurIPS)*, 2023, pp. 29114–29125.

[64] J. M. J. Valanarasu, R. Yasarla, and V. M. Patel, “Transweather: Transformer-based restoration of images degraded by adverse weather conditions,” in *Proc. IEEE/CVF Conf. Comput. Vis. Pattern Recognit. (CVPR)*, 2022, pp. 2353–2363.

[65] B. Li, X. Peng, Z. Wang, J. Xu, and D. Feng, “Aod-net: All-in-one dehazing network,” in *Proc. IEEE/CVF Int. Conf. Comput. Vis. (ICCV)*, 2017, pp. 4770–4778.

[66] X. Xu, R. Wang, and J. Lu, “Low-light image enhancement via structure modeling and guidance,” in *Proc. IEEE/CVF Conf. Comput. Vis. Pattern Recognit. (CVPR)*, 2023, pp. 9893–9903.

[67] S. W. Zamir, A. Arora, S. Khan, M. Hayat, F. S. Khan, M.-H. Yang, and L. Shao, “Learning enriched features for real image restoration and enhancement,” in *Proc. Eur. Conf. Comput. Vis. (ECCV)*, 2020, pp. 492–511.

[68] A. Abdelhamed, S. Lin, and M. S. Brown, “A high-quality denoising dataset for smartphone cameras,” in *Proc. IEEE/CVF Conf. Comput. Vis. Pattern Recognit. (CVPR)*, 2018, pp. 1692–1700.

[69] W. Li, Q. Zhang, J. Zhang, Z. Huang, X. Tian, and D. Tao, “Toward real-world single image deraining: A new benchmark and beyond,” *arXiv preprint arXiv:2206.05514*, 2022.

[70] C. Li, C. Guo, W. Ren, R. Cong, J. Hou, S. Kwong, and D. Tao, “An underwater image enhancement benchmark dataset and beyond,” *IEEE Trans. Image Process.*, vol. 29, pp. 4376–4389, 2020.

[71] Y. Zhou, D. Ren, N. Emerton, S. Lim, and T. Large, “Image restoration for under-display camera,” in *Proc. IEEE/CVF Conf. Comput. Vis. Pattern Recognit. (CVPR)*, 2021, pp. 9179–9188.

[72] Y. Li, Y. Fan, X. Xiang, D. Demandolx, R. Ranjan, R. Timofte, and L. Van Gool, “Efficient and explicit modelling of image hierarchies for image restoration,” in *Proc. IEEE/CVF Conf. Comput. Vis. Pattern Recognit. (CVPR)*, 2023, pp. 18278–18289.

[73] R. Zhang, H. Yang, Y. Yang, Y. Fu, and L. Pan, “Lmhaze: Intensity-aware image dehazing with a large-scale multi-intensity real haze dataset,” in *Proc. ACM Int. Conf. Multimedia Asia (MMAsia)*, 2024, pp. 149–156.

[74] X. Chen, Z. Li, Y. Pu, Y. Liu, J. Zhou, Y. Qiao, and C. Dong, “A comparative study of image restoration networks for general backbone network design,” in *Proc. Eur. Conf. Comput. Vis. (ECCV)*, 2024, pp. 74–91.